NASA/TM—2018-220023

Analysis of the Honeywell Uncertified Research Engine (HURE) With Ice Crystal Cloud Ingestion at Simulated Altitudes: Public Version

Philip C.E. Jorgenson, Joseph P. Veres, Shashwath R. Bommireddy, and Samaun Nili
Glenn Research Center, Cleveland, Ohio

November 2018

NASA STI Program . . . in Profile

Since its founding, NASA has been dedicated to the advancement of aeronautics and space science. The NASA Scientific and Technical Information (STI) Program plays a key part in helping NASA maintain this important role.

The NASA STI Program operates under the auspices of the Agency Chief Information Officer. It collects, organizes, provides for archiving, and disseminates NASA's STI. The NASA STI Program provides access to the NASA Technical Report Server—Registered (NTRS Reg) and NASA Technical Report Server—Public (NTRS) thus providing one of the largest collections of aeronautical and space science STI in the world. Results are published in both non-NASA channels and by NASA in the NASA STI Report Series, which includes the following report types:

- TECHNICAL PUBLICATION. Reports of completed research or a major significant phase of research that present the results of NASA programs and include extensive data or theoretical analysis. Includes compilations of significant scientific and technical data and information deemed to be of continuing reference value. NASA counter-part of peer-reviewed formal professional papers, but has less stringent limitations on manuscript length and extent of graphic presentations.

- TECHNICAL MEMORANDUM. Scientific and technical findings that are preliminary or of specialized interest, e.g., "quick-release" reports, working papers, and bibliographies that contain minimal annotation. Does not contain extensive analysis.

- CONTRACTOR REPORT. Scientific and technical findings by NASA-sponsored contractors and grantees.

- CONFERENCE PUBLICATION. Collected papers from scientific and technical conferences, symposia, seminars, or other meetings sponsored or co-sponsored by NASA.

- SPECIAL PUBLICATION. Scientific, technical, or historical information from NASA programs, projects, and missions, often concerned with subjects having substantial public interest.

- TECHNICAL TRANSLATION. English-language translations of foreign scientific and technical material pertinent to NASA's mission.

For more information about the NASA STI program, see the following:

- Access the NASA STI program home page at http://www.sti.nasa.gov

- E-mail your question to help@sti.nasa.gov

- Fax your question to the NASA STI Information Desk at 757-864-6500

- Telephone the NASA STI Information Desk at 757-864-9658

- Write to:
  NASA STI Program
  Mail Stop 148
  NASA Langley Research Center
  Hampton, VA 23681-2199

NASA/TM—2018-220023

Analysis of the Honeywell Uncertified Research Engine (HURE) With Ice Crystal Cloud Ingestion at Simulated Altitudes: Public Version

Philip C.E. Jorgenson, Joseph P. Veres, Shashwath R. Bommireddy, and Samaun Nili
Glenn Research Center, Cleveland, Ohio

National Aeronautics and
Space Administration

Glenn Research Center
Cleveland, Ohio 44135

November 2018

Acknowledgments

This work is supported by the Advanced Air Transport Technology Project in the NASA Advanced Air Vehicles Program, and is in response to the Engine Icing Technical Challenge. We would like to acknowledge Ashlie Flegel for leading the experimental research test and providing data for the analysis, Dr. Judith Van Zante for providing icing cloud expertise, Dr. William B. Wright (Vantage Partners, LLC.) for guidance in providing the MELT code subroutine, and Dr. Jen-Ching Tsao (Ohio Aerospace Institute) for his insights. The authors would also like to thank the entire NASA PSL staff for their dedication and support of this test. The authors also wish to thank the Honeywell team for their contributions during the engine test.

This work was sponsored by the Advanced Air Vehicle Program
at the NASA Glenn Research Center

Level of Review: This material has been technically reviewed by technical management.

Available from

NASA STI Program
Mail Stop 148
NASA Langley Research Center
Hampton, VA 23681-2199

National Technical Information Service
5285 Port Royal Road
Springfield, VA 22161
703-605-6000

This report is available in electronic form at http://www.sti.nasa.gov/ and http://ntrs.nasa.gov/

Contents

List of Figures

List of Tables

Analysis of the Honeywell Uncertified Research Engine (HURE) With Ice Crystal Cloud Ingestion at Simulated Altitudes: Public Version

Philip C.E. Jorgenson, Joseph P. Veres, Shashwath R. Bommireddy,[1] and Samaun Nili
National Aeronautics and Space Administration
Glenn Research Center
Cleveland, Ohio 44135

Abstract

The Honeywell Uncertified Research Engine (HURE), a research version of a turbofan engine that never entered production, was tested in the NASA Propulsion System Laboratory (PSL), an altitude test facility at the NASA Glenn Research Center. The PSL is a facility that is equipped with water spray bars capable of producing an ice cloud consisting of ice particles, having a controlled particle diameter and concentration in the air flow. In preparation for testing of the HURE, numerical analysis of flow and ice particle thermodynamics was performed on the compression system of the turbofan engine to predict operating conditions that could potentially result in a risk of ice accretion due to ice crystal ingestion. The results of those analyses formed the basis of the test matrix. The goal of the test matrix was to have ice accrete in two regions of the compression system: region one, which consists of the fan-stator through the inlet guide vane (IGV), and region two which is the first stator within the high pressure compressor. The predictive analyses were performed with the mean line compressor flow modeling code (COMDES-MELT) which includes an ice particle model. Together these comprise a one-dimensional icing tool.

The HURE engine was tested in PSL with the ice cloud over the range of operating conditions of altitude, ambient temperature, simulated flight Mach number, and fan speed with guidance from the analytical predictions. The engine was fitted with video cameras at strategic locations within the engine compression system flow path where ice was predicted to accrete, in order to visually confirm ice accretion when it occurred. In addition, traditional compressor instrumentation such as total pressure and temperature probes, static pressure taps, and metal temperature thermocouples were installed in targeted areas where the risk of ice accretion was expected.

The current research focuses on the analysis of the data that was obtained after testing the HURE engine in PSL with ice crystal ingestion. The computational method was enhanced by computing key parameters through the fan-stator at multiple spanwise locations, in order to increase the fidelity with the current mean-line method. In addition, other sources of heat (non-adiabatic walls) were suspected to be the cause of accretion near the splitter-lip and shroud. A simple order of magnitude heat transfer model was implemented into the COMDES-MELT code to estimate the wall temperature minimum and maximum thresholds that support ice accretion, as observed by video confirmation. The results from this model spanned the range of wall temperatures measured on a previous engine that experienced ice accretion at certain operating conditions. Future analyses will require a higher fidelity thermal analysis of the compression system metal walls to accurately calculate the total heat flux to the ice particle. For many data points analyzed, there were differences between the thermodynamic system model and the measured test data that may partially be responsible for uncertainties with the results of the current analyses.

[1]Summer Intern in Lewis' Educational and Research Collaborative Internship Project (LeRCIP)

Nomenclature

Alt	altitude
CD	customer deck
CFM	cubic feet per minute
COMDES	compressor flow analysis code
DeltaISA	offset temperature from ISA
HPC	high pressure compressor
IGV	variable inlet guide vane
ISA	International Standard Atmosphere
IWAR	ice-water flow rate to air flow rate ratio
IWC	ice water content (glaciated ice crystals), g/m^3
LE	leading edge
m	mass flow rate of air, lbm/s
MELT	ice particle thermodynamic state model
N1, N2	fan, HPC rotational speeds
PT1	engine inlet total pressure
Q	air volumetric flow rate, CFM
Tamb	ambient temperature, static
TE	trailing edge
TT1	engine inlet total temperature
Twbs	static wet bulb temperature
TWC	total water content, g/m^3
μ	micron

Introduction

Ice crystals ingested into turbofan engines during the operation of commercial aircraft at high altitudes in high ice water content environments can result in ice accretion in the compression system (Refs. 1 and 2). As ice crystals are ingested into the fan, a portion of the ice crystals melt due to the rising static temperature of the air. It is hypothesized that this ice-water mixture then impacts and cools the surfaces through evaporation and ultimately ice accretes on the components. The accreted ice can cause one or more of the following modes of failure: uncommanded loss of thrust control, compressor surge or stall, ice shedding which can result in structural damage to the compressor blades, and possible combustor flameout. To improve understanding of the causes of ice accretion within an engine, full engine testing with ice crystal ingestion has been performed in the NASA Propulsion Systems Laboratory (PSL) (Refs. 3 to 5), as well as fundamental ice crystal testing (Refs. 6 and 7).

This study focuses on the analysis of the test data obtained from the Honeywell Uncertified Research Engine (HURE). The engine was tested in the PSL with ice crystal cloud ingestion over a range of simulated altitudes and operating conditions. The test took place in January 2018, as part of the engine icing research supported by the NASA Advanced Aircraft Icing Subproject, under the NASA Advanced Air Transport Technology Project. Since the HURE was never in production, it has not had any in-flight events that have been attributed to ice crystal ingestion. The engine was installed into the PSL altitude facility with a direct connect duct that mates to the engine flange, such that it utilizes the full flow capacity of the PSL altitude wind tunnel as illustrated in Figure 1. There was no flight nacelle installed in this test configuration. The PSL is an altitude engine testing facility located at NASA Glenn Research Center. The PSL features the Escort data acquisition system. Each engine data point is stored in the system and is referred to as an Escort data point number. The Escort system records the data at a frequency of approximately one scan per second.

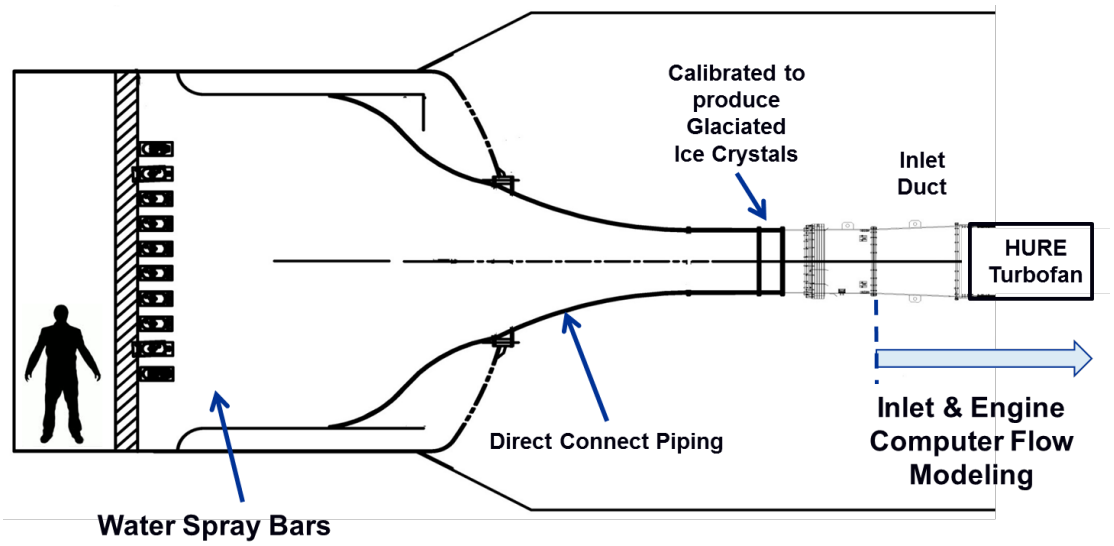

Figure 1.—PSL direct connect inlet duct connects the PSL altitude test facility to engine flange.

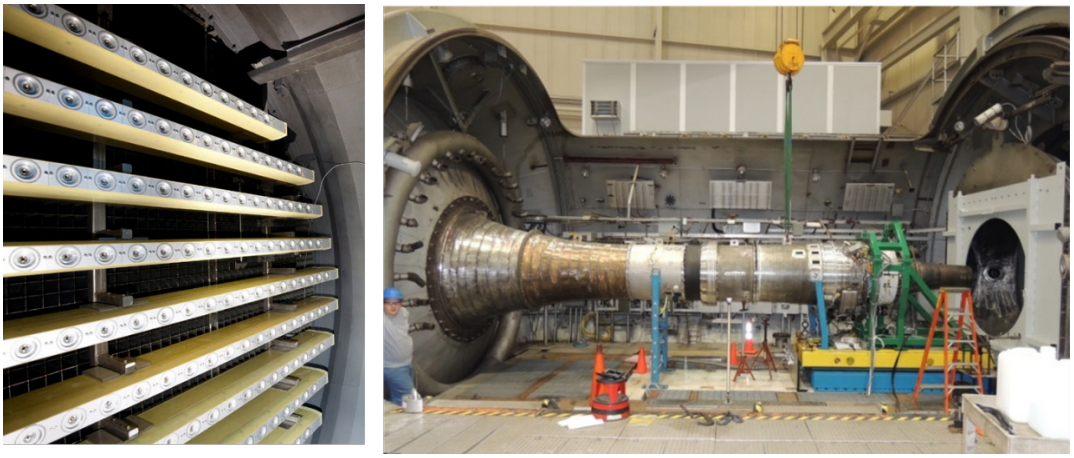

Figure 2.—Full-scale engine testing in PSL-3 at simulated altitude with ice crystal cloud ingestion. The spray bars are shown in the left photo, and the direct connect piping are in the right photo.

This test facility features water spray bars that can produce a fully glaciated ice crystal cloud with controllable ice particle size and concentration per unit volume of air. The spray bars (left photo) and the direct-connect inlet duct piping are shown below in Figure 2 with the engine and test stand (right photo).

The purpose of the test was to determine if ice would accrete within the compressor components at the predicted operating conditions outlined in Reference 8. The HURE engine (cross-section illustrated in Figure 3) was heavily instrumented with traditional pressure and temperature gauges, as well as video cameras at key locations within the compression system.

Prior to the test, an extensive study utilizing a computational tool was performed to determine the operating conditions where a risk of ice accretion would be expected (Ref. 8). The study resulted in numerous operating conditions and altitudes where the ice would be expected to form, at several locations within the compression system. The computational tool that was utilized consisted of an enhanced version of the COMDES mean line compressor flow code (Ref. 9). This tool was previously applied to analyze icing data from other engines tested in PSL with ice crystal ingestion (Refs. 10 to 16). That research resulted in determining values for key parameters that can indicate whether there is a risk of ice accretion. These parameters form the basis of the Icing Wedge. The Icing Wedge is defined by thresholds of static wet bulb temperature, ice-water flow rate to air flow rate, and a non-zero particle melt ratio. Leveraging from the

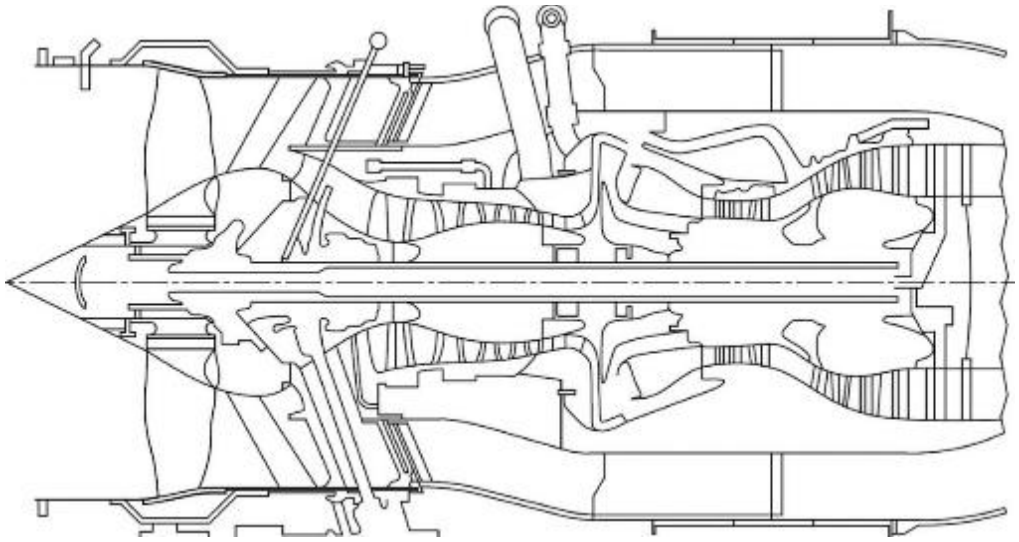

Figure 3.—Honeywell Uncertified Research Engine (Courtesy Honeywell Engines).

previous analytical studies, it was hypothesized in Reference 8 that the Icing Wedge is universally applicable to other turbofan engines. The primary focus of the study in Reference 8 was to determine the engine operating conditions and ambient temperatures at various altitudes, that would result in ice accretion between the fan-stator, splitter-lip, and the inlet guide vane (IGV) of the high-pressure compressor (HPC). The secondary focus of that study was to enable accretion to occur in the variable stator of the HPC first stage (Stator 1). These targeted areas where the ice was expected to occur and the associated station numbers from the compressor flow simulation are illustrated in Figure 4.

The current study is focused on the analysis of 57 Escort test points that were taken at distinct operating conditions in PSL at altitudes between 5K and 45K ft. The computer analyses results for these data points with the Customer Deck as well as with the COMDES-MELT codes are listed in the Appendices A, B, and C in Reference 17. The results of the HURE testing confirmed by the video that ice accreted and, or collected at all altitudes in the general targeted regions of the fan-stator, splitter-lip, and the IGV, confirming most of the predictions made in Reference 8. During testing, it was observed that ice accreted at the fan-stator in accordance with the icing parameter thresholds governed by the Icing Wedge. Note that this fan-rotor is highly loaded, causing a significant rise in total temperature, which is adequate to partially melt the incoming ice particles.

Ice accretion was observed on the front frame components near the splitter-lip at lower static wet bulb temperatures than was expected, based on the Icing Wedge minimum threshold of 492 °R. In addition, the accretion occurred at static air temperatures well below freezing, thus no particle melting could have occurred due to heating from the air alone. The aluminum front frame may have received heat from additional sources besides the air, but this process is not well understood for this engine. It is possible that the ice accretion in that region was not an adiabatic process. During testing, in order to compensate for the lack of a heat transfer model in the COMDES-MELT code, the target static wet bulb temperature (Twbs) for ice to accrete in the front frame region was reduced to 468 °R. This was 24 °R below the Icing Wedge minimum threshold of 492R. The new target Twbs was determined by the analysis of one of the operating points where ice accreted at the splitter-lip and shroud region. Using COMDES-MELT, new testing conditions were rapidly derived prior to further testing, and the test matrix was modified. This was successful in enabling ice to accrete in the front frame components (splitter-lip and shroud region). For post-test data analysis, a simple bulk heat transfer model was developed to estimate the wall metal surface temperature. This was done in order to compare it to previous engine tests which had measured wall temperatures between 493 to 501 °R during ice accretion.

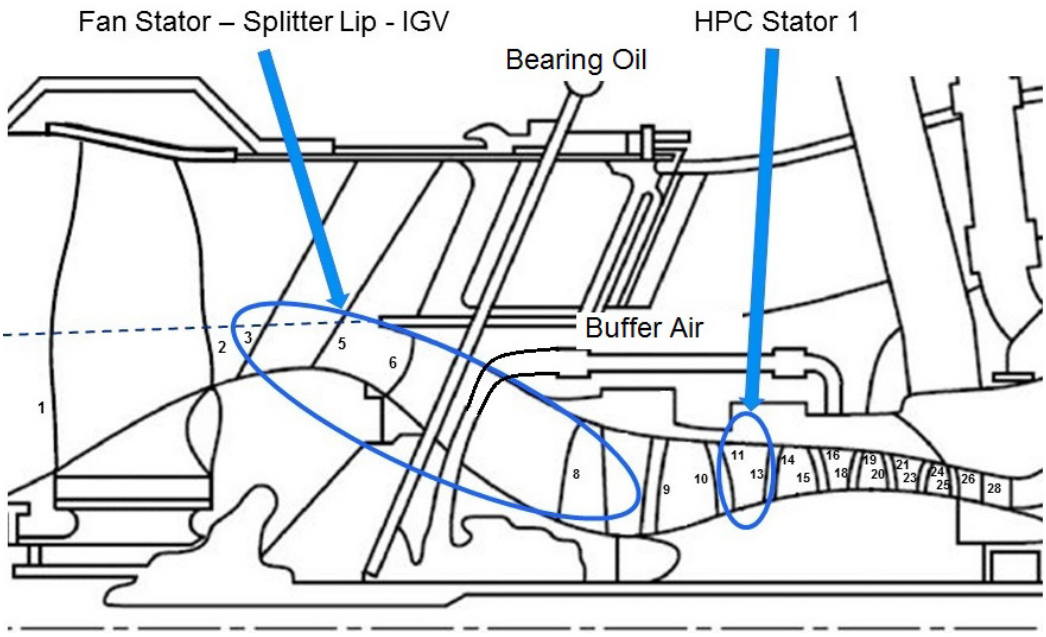

Figure 4.—The targeted locations where the ice was expected to occur are the fan-stator-splitter-lip through IGV, and the HPC Stator 1. Also shown are the associated station numbers used in the compressor flow simulation.

Video observation indicated that ice collected on the variable inlet guide vane (IGV) of the high-pressure compressor. This may have been due to partially melted particles flowing along the shroud wall from upstream, that collected on the IGV surface. This appeared to be different from the ice accretion observed at the upstream regions. Due to the non-adiabatic process upstream of the IGV, the Icing Wedge thresholds, as an indicator of accretion risk, are not applicable in this region.

The test matrix also included three operating conditions where ice was expected to accrete on the HPC variable Stator 1, based on the pre-test analyses. However, during testing it appeared that ice did not accrete there, as evidenced by the measured metal temperatures of the variable Stator 1. There were no video cameras in this region to verify whether ice accreted. Potentially the additional heat source to the particles from the upstream shroud wall near the splitter-lip melted the particles before entering the HPC. The energy imparted by HPC rotor 1 further increased the air temperature, thus raising the mixed-phase “ice-water” temperature entering Stator 1.

The testing of the HURE indicated that ice accreted or collected at all altitudes tested and was confirmed by video cameras at the three targeted locations of fan-stator, splitter-lip-strut, and IGV. Note that the accretion in those locations occurred at different operating conditions. Those test points are superimposed onto the historical engine icing events reported in References 1 and 2, as illustrated in Figure 5. The historical icing events occurred on commercial airlines (Figure 5) during flight through clouds with high ice-water content. Those events have been attributed to ice crystal ingestion and subsequent ice buildup in the engine, but the exact location within the compression system is unknown. The plot in Figure 5 includes reference lines indicating the International Standard Atmosphere (ISA) temperature, with +18 °F and +36 °F above ISA, versus altitude. Ice accretion within the HURE engine spanned the entire range of the reported historical icing events for commercial engines. The PSL test conditions at 5K ft altitude were set to inlet temperatures on the order of –25 °F, which are offset by –45 °F from the ISA temperature, in order to induce ice accretion in the targeted location of the compression system. Note that this condition does not occur in nature, but was artificially set in PSL for icing research and code modeling development.

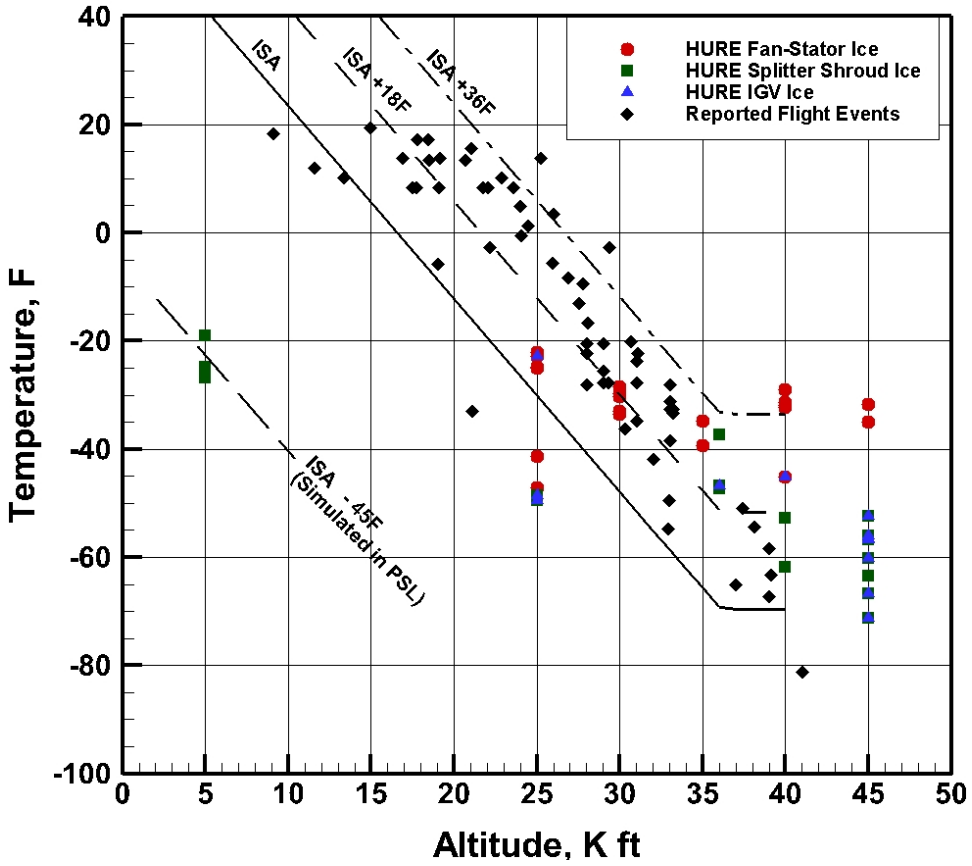

Figure 5.—The confirmed operating points with ice accretion or collection in the HURE engine during PSL testing, superimposed onto the reported commercial engine icing events (Ref. 1).

Post-test analysis showed differences between the engine thermodynamic system model and the measured engine performance data. These comparisons between the system model and the tested engine performance were based on data prior to ice-cloud ingestion. These variances that were on the order of 6% may be partially responsible for uncertainties in the post-test analyses with the COMDES-MELT code, which depends on the engine system model as well as the measured test data for boundary conditions.

Compressor Code Calibration

Prior to testing in PSL, the COMDES code was compared to the design point performance results from a customer deck, as well as more detailed results from a two-dimensional streamline-curvature analysis code for the fan and the four axial compressor stages of the HPC. These two results were provided by Honeywell for the purpose of calibrating the COMDES code at the design point. These are listed in Appendix A of Reference 17, and include the summary of the HURE fan and HPC geometry, as well as the streamline-curvature analysis results, and the COMDES flow code results at each blade edge.

After testing the HURE engine, in order to further verify the accuracy of the COMDES compressor code in being able to model the flow through the full fan and fan-core region, six test data points without ice cloud ingestion were analyzed with the COMDES code (Appendix B of Ref. 17). The purpose was to confirm that the compressor aerodynamic performance predicted by the flow model matched the measured aerodynamic performance test data of the compressor within the engine. In addition to calibrating the rotor and stator losses within the flow model, the effects of the aerodynamic instrumentation installed in the compression system could also potentially influence the measured performance. The effect of the

instrumentation was not significant, since the measured and the fan and compressor aero performance (total temperature and pressure, and static pressure) modeled with the CD and COMDES were all in good general agreement (see Figures 42 to 47 in Appendix B of Ref. 17). Therefore there was no compressor code calibration required to accurately model the fan, flow splitter, and IGV regions. During testing even in an ice cloud environment, it was observed that the total pressure and the wall static pressure measurements in the fan-stator and core strut regions remained unaffected by the particles. However, the cascading aerodynamic effects of small differences in the fan performance can propagate through the HPC and affect the compressor exit conditions (Pt and Tt) through the stage matching. This effect may be responsible for the observed differences in engine performance parameters of up to 6 percent between the CD engine system model and measured Escort test data. Even though the compressor exit plane is well downstream of any ice accretion sites, the differences in conditions there may influence the calculation of core mass flow in the CD system model.

Fan-Stator Analysis; Risk of Accretion Governed by the Icing Wedge Thresholds

The analysis of the HURE test data was performed with the similar computational process shown in Figure 6(a) that was utilized in the predictions of icing risk of Reference 8. The computational process is further detailed in Appendix C of Reference 17, with the description of the input parameters for the engine thermodynamic cycle code (CD) as well as for the COMDES-MELT code. Initially the CD is executed at the tested altitude, ambient temperature, flight Mach number, and fan speed. The results from the engine CD model are utilized as boundary conditions to the subsequent execution of the compressor flow analysis code (COMDES-MELT). The compressor flow analysis is performed to determine the aerodynamic flow field as well as the thermodynamic state of the ice particle, in addition to computing the key icing parameters of wet bulb temperature and IWAR. These analyses assumed that the ice particles would be distributed uniformly through the bypass as well as the engine core, even though this engine has a "hidden core." As part of the ice particle thermodynamic state, the melt ratio is calculated to determine the existence of liquid water content, which is a requirement for there to be ice accretion. Since there is no particle break up model in the code, the analyses was performed over a range of possible particle sizes from 3 to 10 μ. The calculated icing parameters are then compared to the minimum and maximum threshold limits of the Icing Wedge shown in Figure 6(b), and the video images of the compressor components are evaluated to determine if ice accreted on the component. Note that the three-dimensional Icing Wedge shown in Figure 6(b) was derived from a previous turbofan engine test, where the blockage growth rate due to ice accretion was iteratively determined to match the measured wall static pressure and the total pressure ratio. This study only utilizes the minimum and maximum threshold values of the static wet bulb temperature (Twbs) of the Icing Wedge that indicate the risk of accretion on the fan-stator. Estimates of blockage growth rate due to accretion and boundary layer growth are not part of this current study.

The values of the static wet bulb temperature (Twbs) in the fan-stator are utilized as a verification of accuracy for predicting the risk of ice accretion. If the value of Twbs falls between the Icing Wedge thresholds, then there is a risk of ice accretion. The static wet bulb temperature is calculated from the local values of static air temperature and the relative humidity.

The location of ice accretion on the fan-stator was observed in the video to be at discrete radial locations at each operating condition (Escort test point), but for some test points the accretion appeared to be at a higher span than the notional streamline of the fan-core. It became apparent that a full fan flow analysis was also required to determine the Twbs at the higher RMS radius of the full fan.

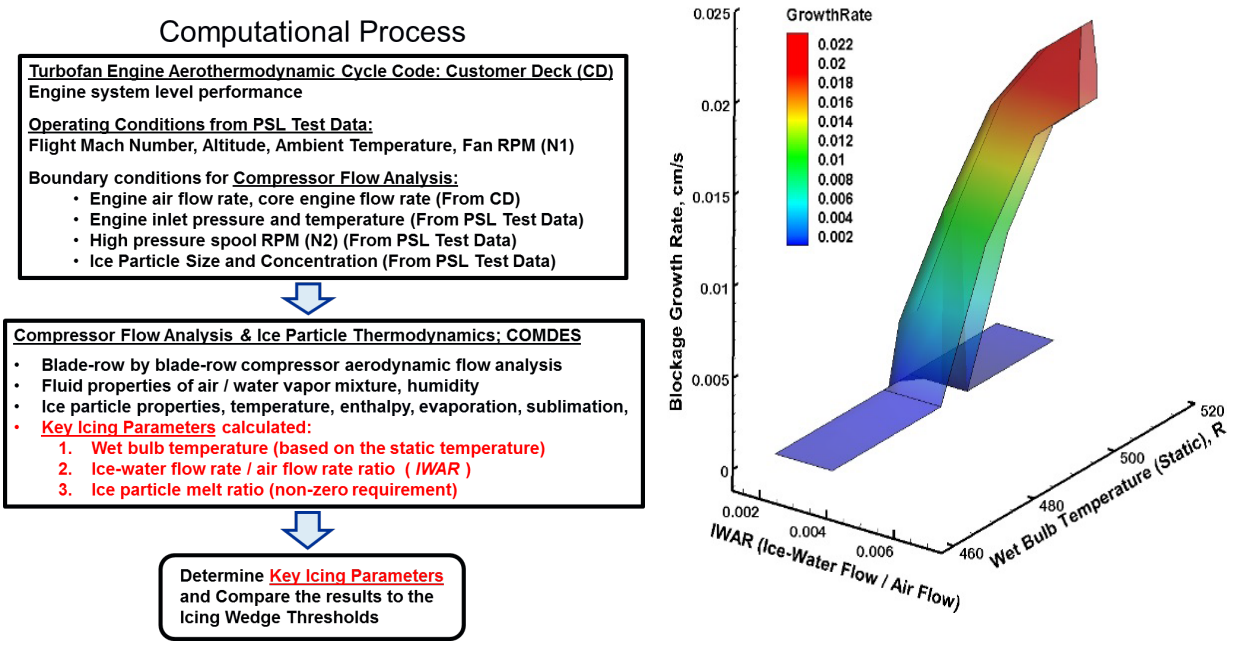

(a) (b)

Figure 6.—(a) Computational process for the test data analysis for the fan stage of the HURE turbofan engine. (b) The Icing Wedge with the thresholds of Twbs between 492 to 498 °R for a risk of accretion.

For this reason two models were created of the fan-stator. The first model was of the full fan-rotor and fan-stator. This analysis resulted in computing the aerodynamic parameters at the root-mean-square (RMS) radius of the full fan stage, as illustrated in Figure 7. The computed parameters included: relative and absolute velocities, static and total pressures and temperatures, absolute and relative flow angles, including the static wet bulb temperature and the particle melt ratio at the leading and trailing edges. The second model was of the fan-core region through the splitter-lip, and the variable IGV. In this analysis, a notional stream line was assumed that divided the flow between the bypass and the core, as illustrated in Figure 7. The notional streamline was used as the fan-core flow path outer wall. Likewise that analysis resulted in modeling all the aerodynamic parameters, including the static wet bulb temperature (Twbs) and the particle melt ratio at the RMS radius of the fan-core stage, through the IGV.

The computed Twbs and IWAR of the Escort test points analyzed in the fan stator region are illustrated in Figure 8. The symbols connected by dotted lines represent the values of Twbs at the full fan and at the fan-core RMS radii. The spanwise work distribution in the fan rotor resulted in a gradient of static temperature, resulting in a large variation of Twbs. The minimum and maximum Twbs thresholds (492 to 498 °R) of the Icing Wedge from Reference 16 are represented by two horizontal lines. These are superimposed onto the calculated values of Twbs obtained from the HURE test data analyses. Figure 8 represents the static wet bulb temperature at Station 5 shown in Figure 7.

The black symbols in Figure 8 indicate the Escort test points where ice accretion on the fan stator was confirmed by video observation. For most of the test points that experienced accretion, the range of Twbs spanned the minimum and maximum thresholds of the Icing Wedge. The combined analysis of the fan-core and full fan results had a 94 percent success rate of spanning the Icing Wedge for all data points analyzed which had ice accretion in the fan-stator.

The test data points where ice accretion was not observed by video in the fan-stator, were outside the Icing Wedge thresholds, as indicated by the red symbols in Figure 8. The analysis results had a 100 percent success rate of being outside the Icing Wedge for all data points analyzed which had no ice accretion in the fan-stator.

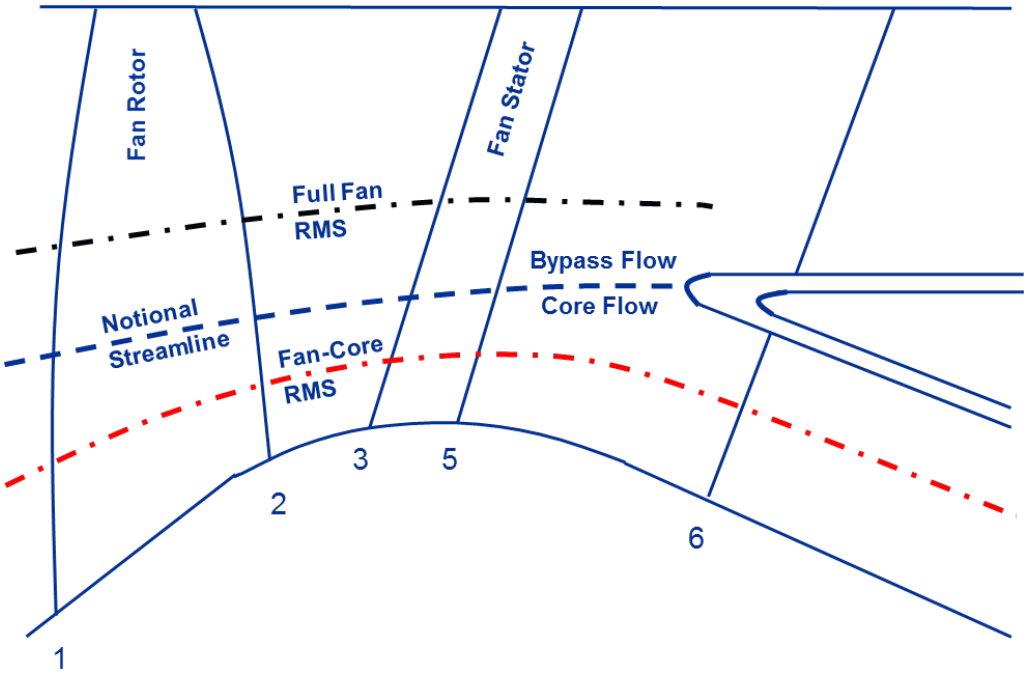

Figure 7.—Two flow models of the fan stage: (a) Full fan; (b) Fan-core, with its outer flow path wall indicated by the notional streamline. The numbers 1 to 6 refer to the meridional stations.

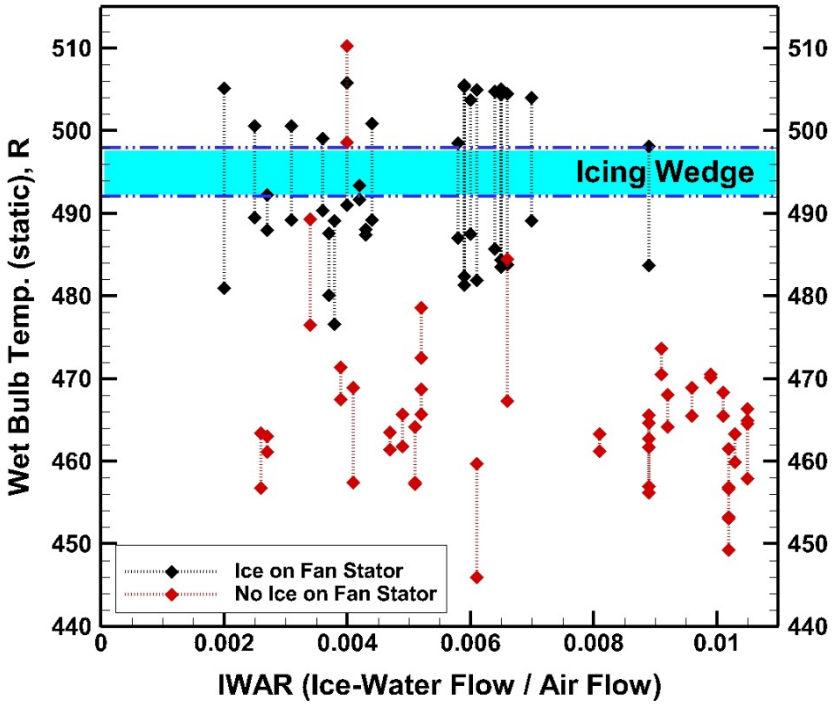

Figure 8.—Range of static wet bulb temperature at the fan-core stator and full fan-stator root-mean-square (RMS) radii.

In summary, there was good agreement between the Twbs thresholds of the Icing Wedge and the analysis of the HURE test results. However, it was necessary to have both the full fan and the fan-core models to determine the range of Twbs along the full span of the fan-stator.

The static wet bulb temperature is based on accurate calculations of the local static air temperature as well as the local relative humidity within the flow field of the fan as well as the four axial stages in the core. A sample data point is shown in Figure 9, where the inlet relative humidity is 100 percent, illustrates the rapid drop in relative humidity. The specific humidity increases due to the sublimation, melting, and evaporation of the ice particles. The accretion at Station 5 (fan-stator trailing edge) occurs at approximately 10 percent relative humidity as shown in Figure 9.

The operating conditions for the Escort data points where there was no ice accretion in the fan-stator are listed in Table 1. All of the data points with no ice accretion were at static wet bulb temperatures below the minimum threshold of 492 °R, except for one (Escort point 212), which was above the Icing Wedge maximum threshold temperature of 498 °R. Escort is the data recording system in PSL. It records the data at a frequency of approximately one scan per second. The computer analyses results for these data points with the Customer Deck as well as with the COMDES-MELT codes are included in Appendix C and listed by Escort number.

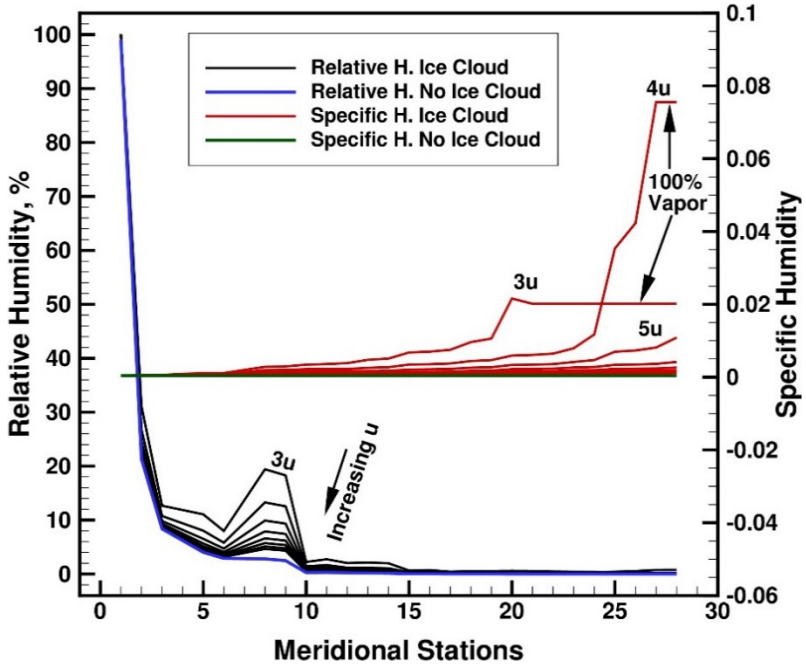

Figure 9.—Distribution of relative and specific humidity through the compression system.

TABLE 1.—FAN-STATOR: NO ICE ACCRETION

Escort data point	Altitude, K ft	Flight Mach Number	Ambient Temp., °R	Delta ISA, °R	Tt PSL Station 1 ice cloud ON, °R	Pt PSL Station 1, psia	Ice Water Content (IWC)	IWAR	Twbs fan core & full fan-Stator, Station 5, 5 μ	Melt ratio, Station 5, 5 μ
147	40	0.62	397.8	7.9	428.5	3.49	1.28	0.0041	457.4 - 468.9	0.0 - 0.0
244	5	0.19	429.8	-71.4	433.1	12.61	10.58	0.0089	462.8 - 461.7	0.0 - 0.0
300	45	0.77	388.3	-1.6	434.2	3.11	2.95	0.0102	453.1 - 453.3	0.0 - 0.0
250	5	0.20	432.8	-68.3	436.2	12.61	5.90	0.0052	472.5 - 478.6	0.0 - 0.0
242	5	0.21	432.9	-68.0	436.9	12.64	10.50	0.0092	468.1 - 464.2	0.0 - 0.0
149	40	0.61	406.9	17.0	437.7	3.49	1.54	0.0049	461.8 - 465.7	0.0 - 0.0
245	5	0.20	434.3	-66.6	437.9	12.60	12.00	0.0101	468.4 - 465.5	0.0 - 0.0
246	5	0.20	434.8	-66.2	438.4	12.61	6.20	0.0052	468.7 - 465.7	0.0 - 0.0
299	45	0.77	392.8	2.9	439.4	3.12	2.92	0.0102	456.7 - 456.9	0.0 - 0.0
279	25	0.60	410.1	-19.6	439.7	6.98	5.80	0.0089	464.7 - 456.2	0.0 - 0.0
280	25	0.60	411.1	-18.5	441.0	6.98	5.80	0.0089	465.6 - 457.0	0.0 - 0.0
282	36	0.61	412.2	22.7	442.6	4.21	1.00	0.0026	463.4 - 456.8	0.0 - 0.0
287	36	0.61	412.2	22.3	443.1	4.22	2.48	0.0066	467.3 - 484.5	0.0 - 0.0
283	36	0.61	412.7	22.8	443.3	4.21	2.00	0.0051	464.2 - 457.3	0.0 - 0.0
284	36	0.61	412.8	22.9	443.4	4.21	4.10	0.0105	464.9 - 457.9	0.0 - 0.0
289	36	0.61	413.5	23.4	443.9	4.21	2.41	0.0061	459.7 - 446.0	0.0 - 0.0
243	5	0.20	440.5	-60.6	444.0	12.61	10.60	0.0091	473.7 - 470.5	0.0 - 0.0
298	45	0.78	396.2	6.4	444.2	3.14	2.95	0.0103	459.9 - 463.3	0.0 - 0.0
293	45	0.77	402.8	12.9	450.5	3.12	2.28	0.0081	463.3 - 461.2	0.0 - 0.0
295	45	0.77	403.1	13.2	450.5	3.13	2.95	0.0102	461.5 - 449.3	0.0 - 0.0
156	45	0.77	403.6	13.7	451.0	3.13	2.73	0.0096	465.5 - 468.9	0.0 - 0.0
291	45	0.77	403.6	13.7	451.4	3.12	0.75	0.0027	463.0 - 461.1	0.0 - 0.0
292	45	0.77	403.1	13.2	451.5	3.12	1.33	0.0047	463.5 - 461.4	0.0 - 0.0
153	45	0.81	399.4	9.5	452.2	3.28	2.89	0.0099	470.2 - 470.5	0.0 - 0.0
157	36	0.61	422.3	32.4	453.6	4.18	1.46	0.0039	471.4 - 467.5	0.0 - 0.0
297	45	0.76	407.2	17.3	454.9	3.12	2.93	0.0105	466.4 - 464.6	0.0 - 0.0
196	30	0.81	427.0	15.8	482.5	6.65	1.92	0.0034	489.3 - 476.5	0.0 - 0.0
212	25	0.80	429.1	-0.4	484.5	8.34	2.60	0.004	498.6 - 510.3	0.20 - 0.41

Figure 10 shows the view of the fan-stator from the video camera mounted on the engine shroud facing radially inward towards the hub. At Escort reading 287 no ice accretion is observed in the fan-stator, and is typical of all the test data points listed in Table 1.

The image shown in Figure 11, is a typical case (Escort 121) where the ice accretion was observed on the fan-stator through the video cameras. All the Escort data points which experienced ice accretion on the fan-stator are listed in Table 2. Eight Escort data points at the bottom of Table 2 (103–209) had significantly less ice accretion than the other data points in the table.

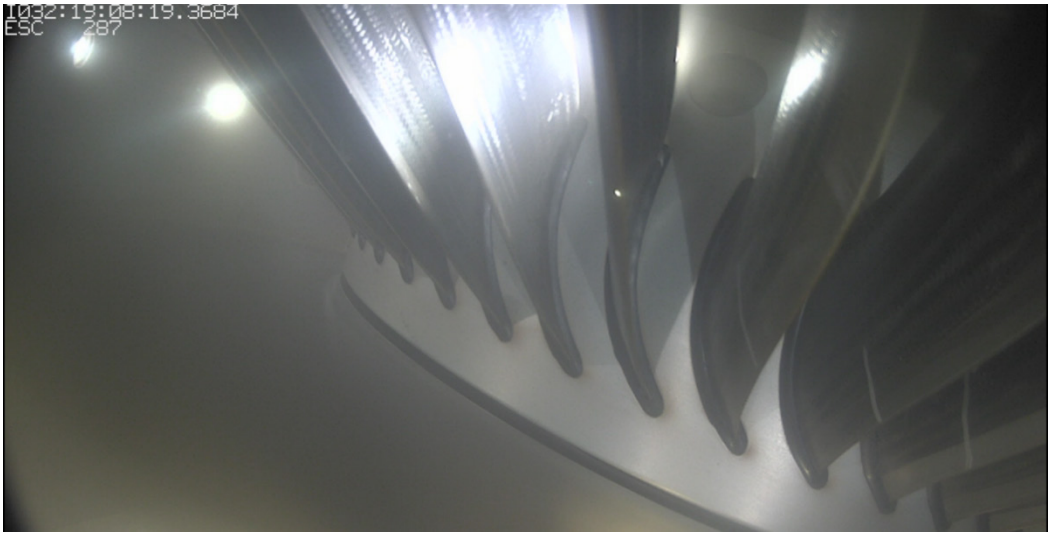

Figure 10.—Video camera view of the fan-stator showing that no ice accretion occurred there during Escort data 287.

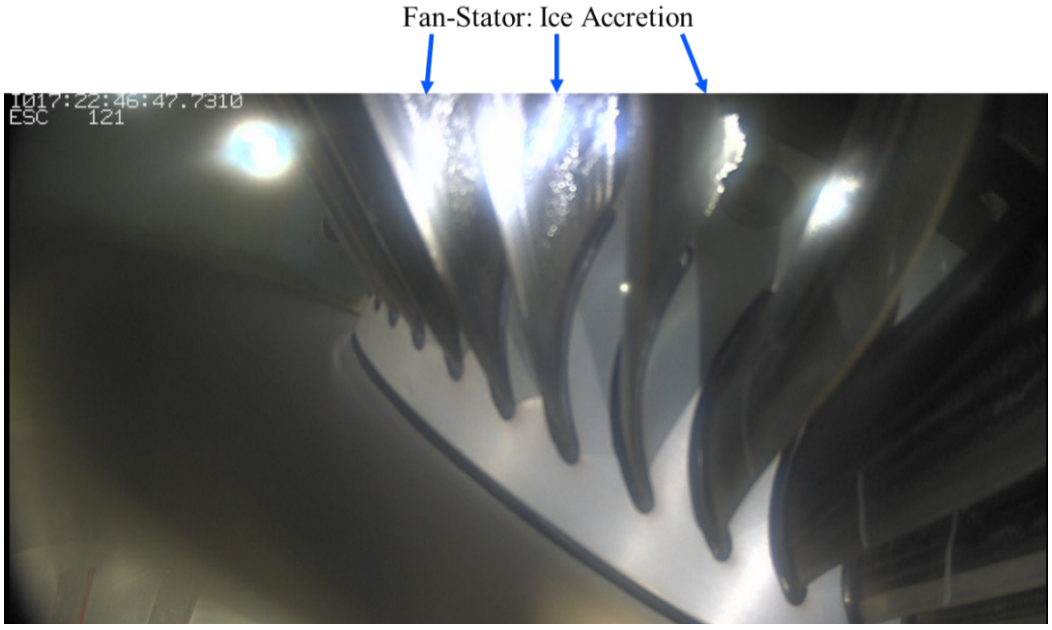

Figure 11.—Video camera view of the fan-stator showing that ice accretion occurred there during Escort data 121.

TABLE 2.—FAN-STATOR: ICE ACCRETION

Escort data point	Altitude, K ft	Flight Mach Number	Ambient temp., °R	Delta ISA, R	Tt PSL Station 1 ice cloud ON, °R	Pt PSL Station 1, psia	Ice Water Content (IWC)	IWAR	Twbs fan core & full fan-stator, Station 5, 5 μ	Melt fatio, Station 5, 5 μ
100	25	0.40	436.7	10.4	450.9	5.86	2.93	0.0061	481.9 - 505.0	0.0 - 0.28
276	25	0.41	436.8	7.3	451.3	6.12	2.93	0.0059	481.4 - 505.4	0.0 - 0.28
187	25	0.41	437.5	7.9	451.9	6.12	2.93	0.0059	482.4 - 505.5	0.0 - 0.283
193	30	0.61	429.3	18.2	461.1	5.56	2.89	0.0065	483.5 - 504.4	0.0 - 0.27
122	30	0.60	429.9	18.4	461.2	5.57	2.88	0.0065	484.4 - 505.1	0.0 - 0.0
191	30	0.61	429.9	18.7	461.7	5.57	2.90	0.0066	483.8 - 504.5	0.0 - 0.271
188	30	0.60	431.1	19.8	462.7	5.57	2.84	0.0064	485.7 - 504.8	0.0 - 0.283
214	25	0.81	412.4	-16.9	466.0	8.34	4.00	0.006	487.5 - 503.7	0.006 - 0.17
123	40	0.81	414.5	24.6	469.3	4.08	2.90	0.0089	483.7 - 498.1	0.0 - 0.107
124	35	0.81	420.3	27.3	475.2	5.25	2.89	0.007	489.1 - 504.0	0.019 - 0.272
108	35	0.80	424.8	31.7	479.9	5.25	1.52	0.0036	490.4 - 499.1	0.03 - 0.114
114	40	0.81	428.3	38.4	484.2	4.09	1.42	0.0044	489.2 - 500.9	0.02 - 0.22
121	45	0.81	427.9	38.0	484.4	3.28	1.48	0.0058	487.0 - 498.5	0.0 - 0.16
118	40	0.82	427.7	37.9	485.7	4.08	1.46	0.0043	488.1- 487.4	0.0 - 0.0
103	25	0.65	434.7	5.0	471.7	7.27	2.50	0.0042	491.7 - 493.4	0.037 0.002
105	25	0.65	434.5	4.9	471.8	7.28	2.36	0.0037	487.6 - 480.1	0.0 - 0.0
213	25	0.80	418.3	-11.3	472.3	8.35	2.60	0.004	491.0 -505.8	0.05 - 0.24
159	45	0.76	424.6	34.7	473.6	3.12	0.50	0.002	481.0 - 505.2	0.0 - 0.0
110	30	0.81	426.0	14.8	481.6	6.66	1.95	0.0027	492.3 - 488.0	0.053 - 0.00
112	30	0.80	426.7	15.1	481.7	6.66	2.20	0.0038	489.1 - 476.6	0.0 - 0.0
208	40	0.83	427.3	37.4	485.6	4.08	1.00	0.0031	489.2 - 500.6	0.021 - 0.22
209	40	0.80	430.6	40.7	486.1	4.08	0.80	0.0025	489.5 - 500.6	0.028 - 0.22

Figure 12 illustrates the static wet bulb temperature distribution through the full fan (represented by blue lines), and the fan-core and the four stage axial compressor (represented by black lines), as well as the particle melt ratio over a range of particle size from 3 to 10 μ.

The computer analyses results for these data points listed in Table 2 are included in Appendix C of Reference 17, listed by Escort number. Table 1 and Table 2 show the static wet bulb temperature and the corresponding particle melt ratio for a 5 μ particle at the trailing edge of the fan-stator (Station 5 in Figure 4 and Figure 7). However a range of particle sizes were analyzed with the COMDES-MELT code between 3 and 10 μ for all the stations in the flow path. The full fan model had 5 meridional stations, while the fan-core model is comprised of 28 meridional stations, as shown in Figure 2, since the four axial stages of the high pressure compressor were also included as part of the flow analysis. The calculated Twbs downstream of the HPC rotor 1 (meridional station 9) was significantly higher than the maximum threshold of the Icing Wedge. Therefore there was no risk of accretion in the downstream stages, although there were no video cameras in those stages for visual confirmation. For the Escort data points where ice accretion occurred on the fan-stator, there was no accretion observed concurrently on the splitter-lip, shroud, strut, IGV regions. Likewise, when ice accretion was observed in the splitter-lip, shroud, strut, IGV regions, there was no accretion observed concurrently on the fan-stator.

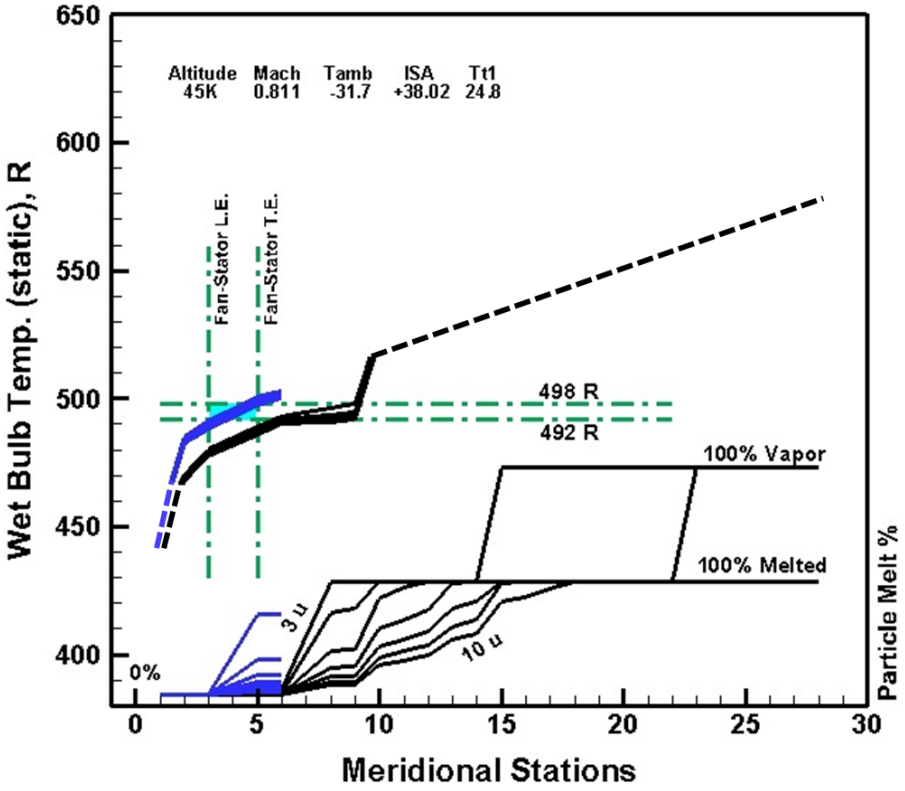

Figure 12.—Ice accretion occurred in the fan-stator during Escort 121. The static wet bulb temperature was within the Icing Wedge.

Splitter-Lip-Strut-Gooseneck Region; Non-Adiabatic Wall

PSL Test, and Real-Time Predictions of Ice Accretion Operating Points

Early in the HURE testing, it was observed that at several of the tested operating points, ice accretion in the front frame region (splitter, shroud, gooseneck and support strut) did not occur as expected even though the static wet bulb temperatures (Twbs) were within the thresholds of the Icing Wedge. Although there were no metal thermocouples to measure the wall temperature near the aluminum splitter-shroud region, it is assumed that the metal temperatures were above freezing, since liquid water streaks were observed in the videos on the shroud. The target static wet bulb temperature was reduced by 24 °R from the Icing Wedge minimum threshold value of 492 °R in order to accrete ice in the region of the front frame. The value of 468 °R was determined through flow modeling in near real-time analysis of several test data points that experienced ice accretion at the splitter-shroud region. Flow analysis of those data points indicated that the calculated static air temperature was well below freezing at this location. Thus no melting could have possibly occurred solely due to the heat of compression caused by the fan. In addition, the calculated temperature of the ice particles was also well below freezing, based on the flow analysis.

New testing operating conditions over a wide range of simulated altitudes were rapidly determined utilizing the lower Twbs threshold in the splitter-shroud region prior to further testing, and the test plan was modified accordingly. With these updated conditions ice began to accrete within seconds after the ice cloud was initiated. It was assumed that the splitter-shroud region wall temperatures at this condition were near freezing, since the measured metal temperatures on the IGV were at freezing. This technique was successful in inducing ice to accrete in the splitter-shroud region, for most subsequent tested operating points. Note that when ice accretion was observed in the splitter-lip-strut, shroud region there was no accretion observed on the fan-stator at the same operating points.

The aluminum front frame may have received heat from additional sources besides the air, in order to partially melt the particles, which then subsequently accreted near the splitter-lip-shroud. A physics-based explanation was sought for this phenomenon. It is possible that the ice accretion in this region is due to a non-adiabatic wall. Although the source of additional heat flux is not completely understood, a simple order-of-magnitude heat flux model was implemented in COMDES-MELT to estimate the wall temperature in this region.

Order-of-Magnitude Estimate of Wall Temperature

In order to reconcile the additional enthalpy from the non-adiabatic flow path wall, an order-of-magnitude method was implemented that assumes a continuous supply of heat which is transferred directly to the ice particle by conduction. The heat transfer model was calibrated empirically based on the HURE test results. Since there were no thermocouples in the splitter-shroud region of the front frame where ice accreted, it was necessary to utilize measured IGV metal temperature test data to develop the heat transfer model for the front frame. The purpose of the heat transfer model was to calculate the wall temperature in the splitter-shroud region. Several data points were observed to have glassy ice accretion at the splitter-lip and shroud of the gooseneck with no shedding (hard ice). At these operating points it was observed that the measured metal temperatures at the IGV were near 492 °R. It was therefore assumed that the metal temperature at the splitter-lip and shroud were likewise near 492 °R at these operating conditions. Table 3 below lists four test data points at various altitudes that were used to confirm that when hard ice was observed to accrete on the splitter-lip and (or) the shroud, the IGV had a measured metal temperature near 492 °R. This was also observed in the previous engine test (Ref. 15 see Figures 14 and 15). The total air temperature at the splitter-shroud region was approximately the same in the CD and COMDES models, and confirmed by the measured Escort data. The calculated static air temperature in the splitter-shroud region as modeled by COMDES was consistently below freezing. Yet it was observed that ice accreted in the splitter-strut-shroud region.

TABLE 3.—DATA POINTS UTILIZED TO CALIBRATE HEAT TRANSFER MODEL IN COMDES-MELT

Test data point (Escort)	Altitude, K ft	Splitter-shroud total air, CD, escort and COMDES, °R	Splitter-shroud tstatic air CD, COMDES, °R	Tigv metal pre ice cloud, °R	Tigv metal post ice cloud; after 60 sec, °R
156	45	509.4	486.3	511.2	492.3
283	36	499.9	481.9	501. 1	491.0
279	25	496.1	478.1	494.2	491.9
242	5	492.8	476.9	492.0	491.9

A simple heat transfer model was created, where the initial unknown was the bulk heat transfer coefficient at the splitter-shroud flow path wall, $h_{wall\ plenum}$. To estimate $h_{wall\ plenum}$, two of the test data points were selected (156 and 283) which had visual confirmation of glassy, hard ice accretion which did not shed, on the splitter-lip and shroud. Although the exact source of heat (enthalpy) to the walls was not known, in this study it is assumed that the heated air from a downstream stage was the source. In order to have this additional enthalpy vary with engine operating conditions, for modeling purposes it was assumed that the source was the HPC stage 2 exit (COMDES; *Tt2*).

In the analysis that follows, the temperature of the plenum, $T_{wall\ plenum}$, was assumed to be the same as *Tt2*. At the selected data points (156 and 283), the heat flux, Q, was calculated assuming that the splitter and shroud wall temperatures, $T_{wall\ core}$, were at 492 °R with the following Equation (1), where the m is the mass flow rate of the ice particles going through the engine core.

$$Q = SHC * m * (T_{particle} - T_{wall\ core}) \tag{1}$$

The mass flow of ice particles through the engine core is assumed to be proportional to the air flow rate, since the compressor code lacked a model to track the particles within the flow path in three-dimensional space. The *SHC* is the specific heat capacity of the ice particles. The ice particle temperature was obtained from an initial solution of the COMDES-MELT code. Knowing the heat flux, Q, the temperature on the plenum side of the shroud wall, $T_{wall\ plenum}$, was computed with Equation (2).

$$T_{wall\ plenum} = Q * \frac{Thickness}{(A*k)} + T_{wall\ core} \tag{2}$$

The A in the above equation is the surface area of the splitter-shroud region through the entire goose neck, while k is the coefficient of conduction for aluminum, and thickness is the average wall thickness of the aluminum shroud casing. The bulk heat transfer coefficient, $h_{wall\ plenum}$ was determined for this engine based on the assumption of wall temperature of 492 °R with Equation (3).

$$h_{wall\ plenum} = \frac{Q}{A*(T_{wall\ plenum} - T_{air\ plenum})} \tag{3}$$

For the flow analysis of all other data points, the bulk heat transfer coefficient was assumed to remain at the value which was calculated from the data points 156 and 283 of Table 3. The above three equations were incorporated into COMDES-MELT and are solved for the three unknown parameters (Q, $T_{wall\ plenum}$, $T_{wallcore}$) for all subsequent data points analyzed in this study. COMDES-MELT was executed iteratively to first, determine $T_{wall\ plenum}$ *(Tt2)* and particle temperature at the splitter–shroud region, and finally

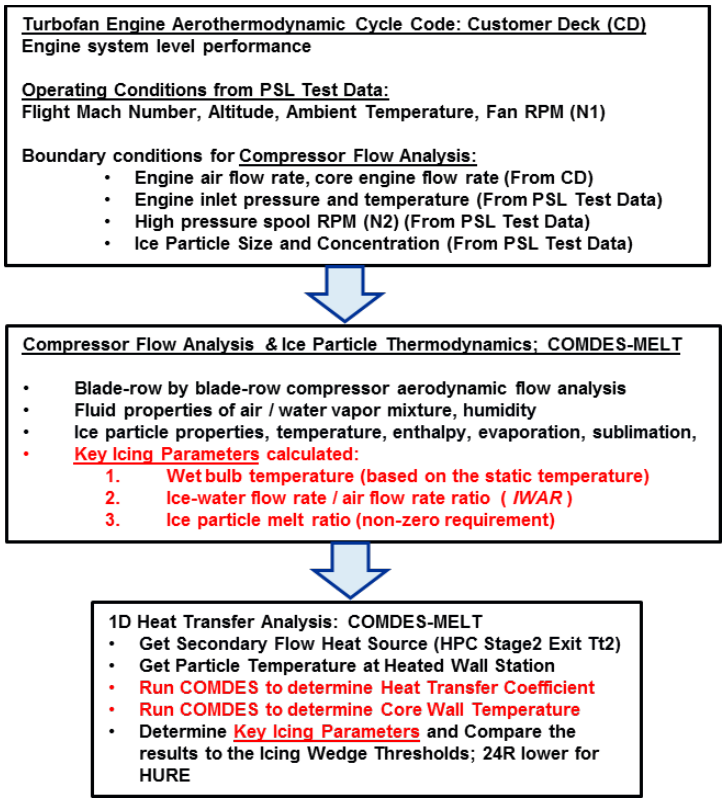

Figure 13.—Computational Process for Non-Adiabatic Walls that was incorporated into the COMDES-MELT code to estimate the core wall temperature at the splitter-shroud region.

executed to calculate the splitter–shroud wall temperature ($T_{wall\ core}$). However, in the current study the enthalpy extracted from the heated wall was not transferred back to the ice particle to determine its thermodynamic state once it made contact with the heated splitter-shroud wall. The computational process summarizing the steps above is outlined in Figure 13 and in Appendix C of Reference 17.

The computed value of $T_{wall\ core}$ was then compared to previous engine test data (Honeywell ALF502R-5, serial number LF11) with measured wall metal temperatures at the location where there was significant ice accretion (Ref. 15) and are illustrated in Figure 14. Note that additional analysis of the engine data in Reference 15 was performed as part of this study, and is illustrated in Figure 14. Ice accretion occurred on the LF11 compressor shroud wall at measured metal temperatures on the shroud wall between 493 and 501 °R.

The $T_{wall\ core}$ calculations for all HURE test data points which were analyzed are illustrated in Figure 15. The range of calculated metal wall temperatures at the splitter-shroud region using the heat transfer model described above where ice accretion was confirmed by video, were between 475 to 519 °R, and span the range of wall temperatures measured in the LF11 engine during accretion. The calculated HURE wall temperatures were superimposed onto the measured wall temperatures of the LF11 engine in Figure 15. The figure illustrates LF11 metal temperatures that supported accretion, as well as a few data points where accretion was not observed.

During the HURE testing it was observed through video confirmation that there were two distinct types of ice accretion at the splitter-shroud region, which did not shed. These are what were defined as “ice accretion” and appeared to be glassy and fully transparent, and are plotted in Figure 15 and Figure 16 with solid blue circles. An example of each of these two types of ice accretion is highlighted in the following section.

The first type of distinct ice accretion occurred on the splitter-lip at discrete circumferential locations, and often had protruding horn shapes growing upstream, as shown in Figure 17.

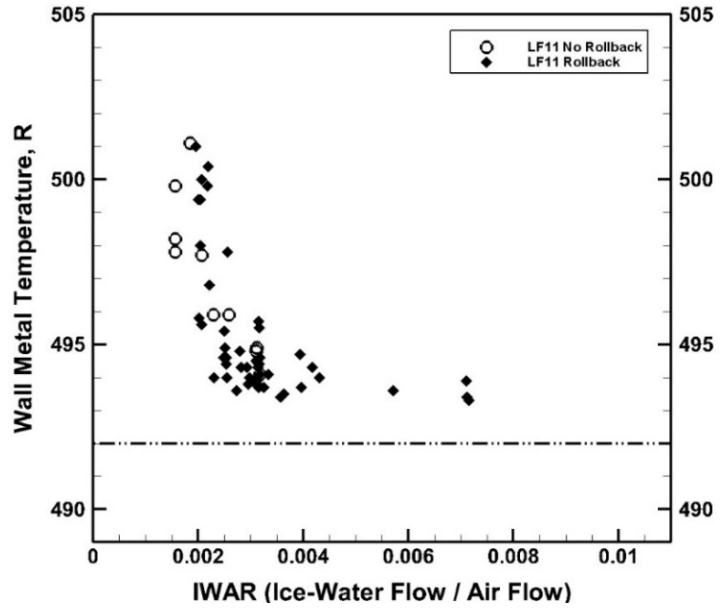

Figure 14.—Honeywell ALF502, serial LF11 measured wall temperatures with video confirmed ice accretion. The closed symbols resulted in engine rollback, while the open symbols had ice but did not result in engine rollback. (Ref. 15).

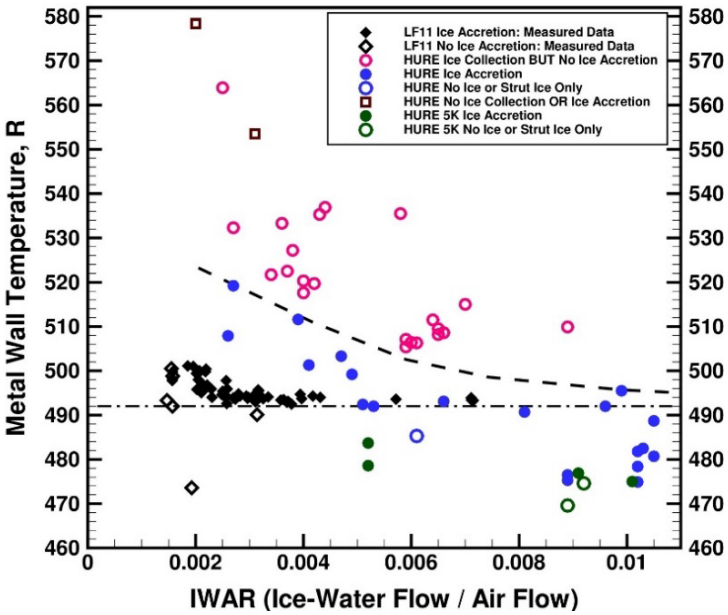

Figure 15.—Calculated wall metal temperature of the HURE splitter-shroud region, compared to the measured wall temperature of the LF11 engine (Ref. 15), versus IWAR.

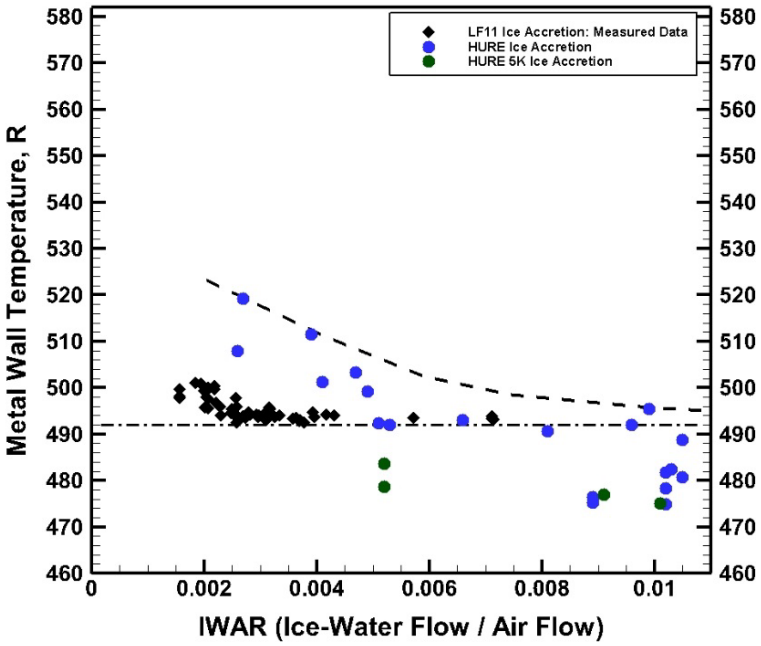

Figure 16.—Calculated wall temperature versus IWAR of the HURE splitter-shroud region for data points with ice accretion at high altitudes and at 5K ft, compared to the measured wall temperature of the LF11 engine (Ref. 15).

Figure 17.—Escort 153. Ice accretion with ice horns on the splitter.

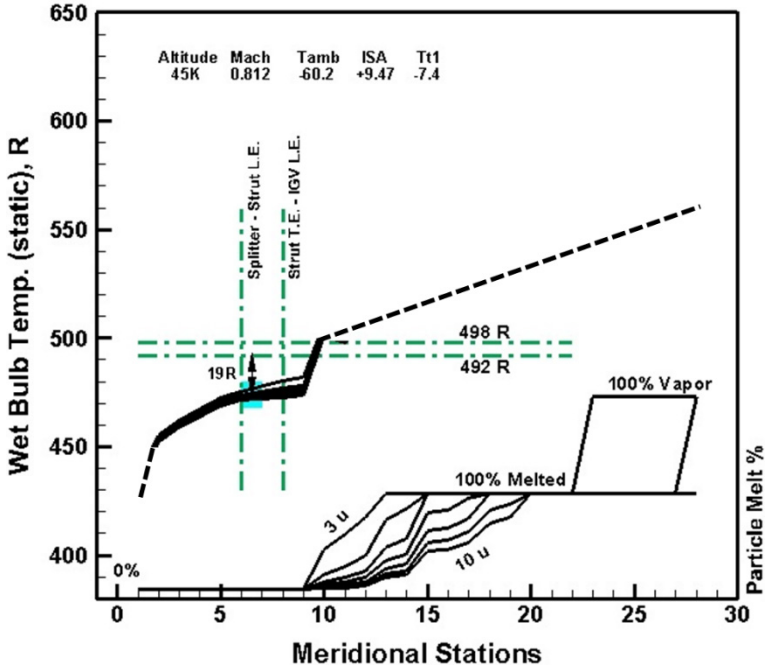

Figure 18.—Ice accretion occurred at the splitter shroud during Escort 153. The static wet bulb temperature is 19 °R below the Icing Wedge minimum threshold of 492 °R.

For Escort data point 153, the compressor flow model was executed to determine the static wet bulb temperature distribution through the full fan, the fan-core and the four stage axial compressor, as well as the particle melt ratio over a range of particle size for 3 to 10 μ, and is illustrated in Figure 18. The results of the flow analysis for this data point indicated that the static wet bulb temperature at the splitter-shroud region was 19 °R below the Icing Wedge minimum threshold.

Escort data point 156 is an example of the second distinct type of ice accretion in the splitter-shroud region in which ice accreted on the shroud surface but without ice horns on the splitter, and is shown in Figure 19. For Escort data point 156, the compressor flow model was executed to determine the static wet bulb temperature distribution through the full fan, the fan-core and the four stage axial compressor, as well as the particle melt ratio over a range of particle size for 3 to 10 μ, and is illustrated in Figure 20. The flow model indicated that the splitter-lip-shroud surface wet bulb temperature was 24 °R below the Icing Wedge minimum threshold of 492 °R.

Figure 19.—For Escort 156, there was ice accretion on the shroud, without horns.

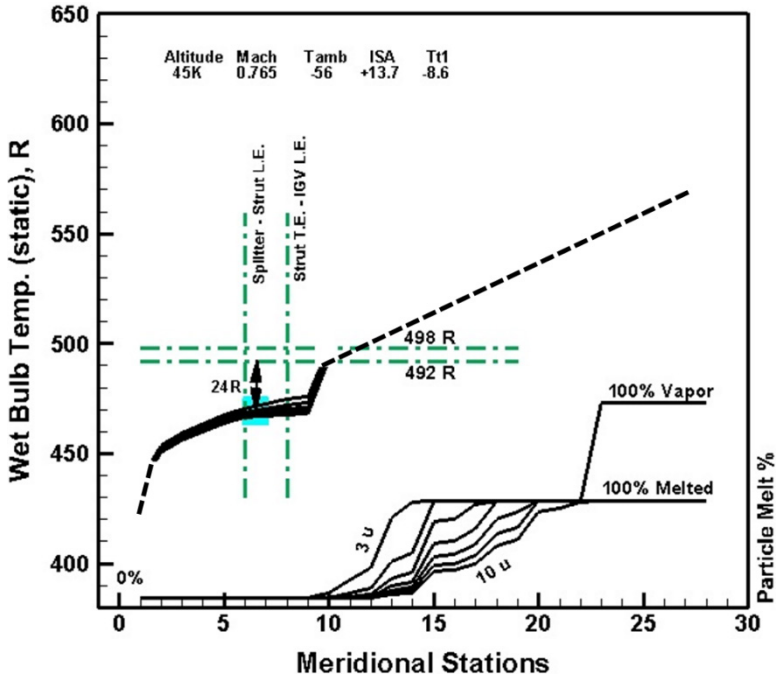

Figure 20.—Ice accretion occurred at Escort 156. The static wet bulb temperature is 24 °R below the Icing Wedge minimum threshold of 492 °R.

For all data points experiencing ice accretion, key aerodynamic and icing parameters are listed in Table 4. The computer analyses results for these Escort data points with the Customer Deck as well as with the COMDES-MELT codes are included in Appendix C of Reference 17 and listed by Escort number.

TABLE 4.—SPLITTER-SHROUD: ICE ACCRETION DATA POINTS

Escort data point	Altitude, K ft	Flight Mach	Ambient temp., °R	Delta ISA, °R	Tt PSL Station 1 ice cloud ON, °R	Pt PSL Station 1, psia	Ice Water Content (IWC)	IWAR	Twbs splitter, shroud, fan core (6), 5 μ	Ice mass flow into core, lbm/sec	Kinetic energy heat flux, Qk	Conduct heat flux, Qc, BTU/Hr	Total heat flux, Qt, BTU/Hr	T wall core after 60s (6) 2.1, °R	T ice particle (6) 2.1, °R
147	40	0.62	397.8	7.9	428.5	3.49	1.28	0.0041	462.5	0.047	0.292	3626	3626	501.3	458.3
300	45	0.77	388.3	-1.6	434.2	3.11	2.95	0.0102	456.6	0.084	0.404	3250	3251	474.9	453.5
149	40	0.61	406.9	17.0	437.7	3.49	1.54	0.0049	465.5	0.049	0.263	3289	3289	499.2	462.2
299	45	0.77	392.8	2.9	439.4	3.12	2.92	0.0102	460.1	0.085	0.417	3267	3267	478.4	457.0
279	25	0.60	410.1	-19.6	439.7	6.98	5.80	0.0089	467.9	0.155	0.650	2818	2818	475.3	465.2
280	25	0.60	411.1	-18.5	441.0	6.98	5.80	0.0089	468.8	0.153	0.645	2866	2867	476.5	466.1
282	36	0.61	412.2	22.7	442.6	4.21	1.00	0.0026	466.0	0.026	0.104	2070	2070	507.9	463.5
287	36	0.61	412.2	22.3	443.1	4.22	2.48	0.0066	471.5	0.085	0.498	3845	3846	493.1	467.9
283	36	0.61	412.7	22.8	443.3	4.21	2.00	0.0051	466.8	0.052	0.207	2618	2618	492.4	464.3
284	36	0.61	412.8	22.9	443.4	4.21	4.10	0.0105	467.5	0.106	0.426	2997	2997	480.7	465.1
298	45	0.78	396.2	6.4	444.2	3.14	2.95	0.0103	463.1	0.084	0.407	3390	3390	482.5	460.2
293	45	0.77	402.8	12.9	450.5	3.12	2.28	0.0081	466.2	0.064	0.297	3109	3109	490.7	463.5
295	45	0.77	403.1	13.2	450.5	3.13	2.95	0.0102	463.2	0.063	0.200	2340	2340	481.8	461.3
156	45	0.77	403.6	13.7	451.0	3.13	2.73	0.0096	467.9	0.073	0.314	3273	3273	492.0	467.1
292	45	0.77	403.1	13.2	451.5	3.12	1.33	0.0047	466.3	0.037	0.174	2651	2651	503.3	463.6
153	45	0.81	399.4	9.5	452.2	3.28	2.89	0.0099	473.1	0.088	0.441	3995	3995	495.5	470.3
157	36	0.61	422.3	32.4	453.6	4.18	1.46	0.0039	474.1	0.041	0.182	2928	2928	511.6	471.6
297	45	0.76	407.2	17.3	454.9	3.12	2.93	0.0105	469.2	0.082	0.391	3286	3286	488.7	466.6

The range of static wet bulb temperatures of the Icing Wedge for these ice accretion points was from 456.6 to 474.1 °R with a 5 μ particle in the flow analysis model. The average difference of the Twbs for these ice accretion points was 25 °R below the 492 °R minimum threshold Twbs of the Icing Wedge, with a range of 17.5 °R (see Figure 24). Note that due to the additional heat from the splitter-shroud region, the Twbs threshold for hard ice accretion is significantly below the 492 °R of the Icing Wedge for this engine.

It was also observed through video that on many test data points ice would collect on the splitter-lip but would rapidly shed at up to 3 sheds per second. This type of ice was not glassy, but rather appeared to be white and not transparent. These data points are referred to as "ice collection" data points in this study, since they did not appear to adhere to the surface, but rather the ice-water particles appeared to have been merely collected at the splitter-lip stagnation point, and rapidly shed. These data points are illustrated as open pink circles in Figure 15 and Figure 21. As evident from Figure 21 these data points with rapid shedding occurred at conditions that were at warm metal temperatures, as calculated with the heat transfer model in the compressor code.

A typical data point featuring ice collection on the splitter-lip with rapid shedding is shown in Figure 22. The ice collection appear as small white ice "mounds" which were quite different from the glassy hard ice noted in the previous ice accretion cases. These mounds appeared at circumferentially discrete locations on the splitter lip, and shed at a rapid rate of from multiple times per second to several seconds per shed. The calculated metal temperatures for these data points were in the range from 505.4 to 563.9 °R. These were well above the maximum measured wall temperatures of 501 °R that supported ice accretion from Reference 15.

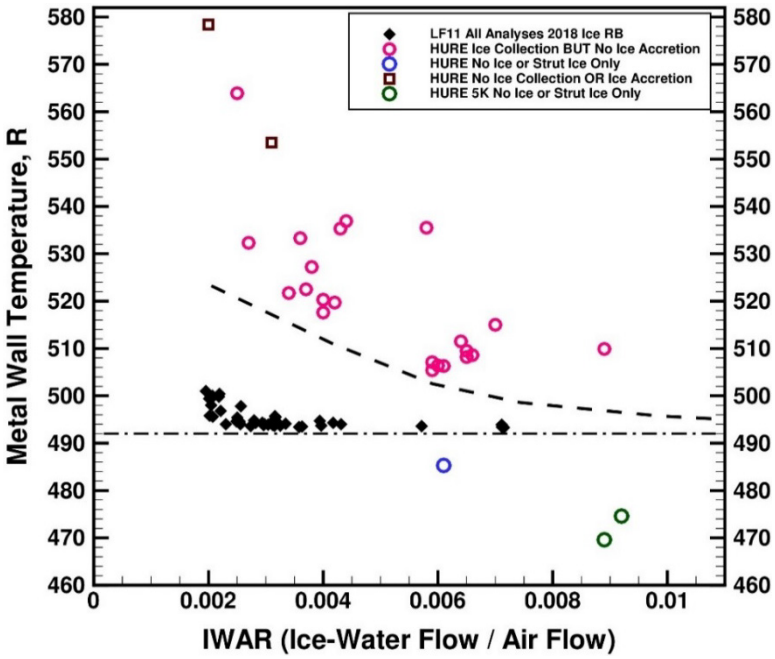

Figure 21.—Calculated wall temperature versus IWAR of the HURE splitter-shroud region with no ice accretion, only ice collection and rapid shedding. Black symbols are the measured wall temperatures at the location of ice accretion (Ref.15).

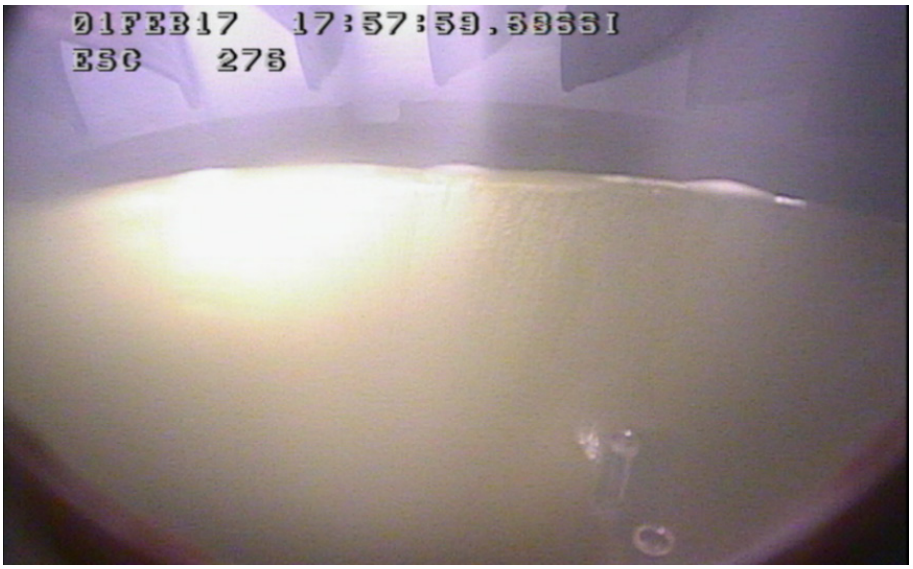

Figure 22.—Ice collection on the splitter-lip with rapid shedding, is not considered ice accretion since it does not grow (Escort 276).

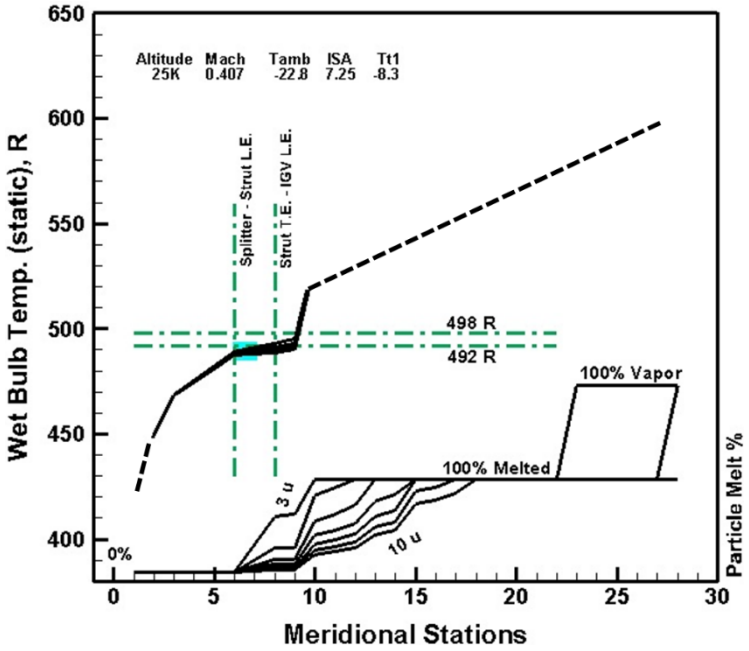

Figure 23.—Ice accretion did not occur for Escort point 276 due to additional heat from the warm wall at the stator-shroud region. The static wet bulb temperature there was on the order of 487.9 °R.

Figure 23 illustrates the static wet bulb temperature distribution for Escort points 276 through the full fan, the fan-core and the four stage axial compressor, as well as the particle melt ratio over a range of particle size for 3 to 10 μ. Ice accretion did not occur at the stator-shroud region due to the additional heat from the splitter-shroud wall, as the wet bulb temperature was 5 °R below the Icing Wedge minimum threshold limit.

For data points that experienced ice collection with rapid shedding, but no ice accretion, the key aerodynamic and icing parameters are listed in Table 5. The full analysis results for these Escort data points with the Customer Deck as well as with the COMDES-MELT codes are included in Appendix C of Reference 17 and listed by Escort number.

TABLE 5.—SPLITTER-SHROUD: ICE COLLECTION WITH RAPID SHEDDING; NO ACCRETION (CALCULATED HOT WALL)

Escort data point	Altitude, K ft	Flight Mach	Ambient temp., °R	Delta ISA, °R	Tt PSL Station 1 ice cloud ON, °R	Pt PSL Station 1, psia	Ice Water Content (IWC)	IWAR	Twbs splitter, shroud, fan core (6), 5 μ	Ice mass flow into core, lbm/sec	Kinetic energy heat flux, Qk	Conduct heat flux, Qc, BTU/Hr	Total heat flux, Qt, BTU/Hr	T wall core after 60s (6) 2.1, °R	T ice particle (6) 2.1, °R
100	25	0.40	436.7	10.4	450.9	5.86	2.93	0.0061	487.9	0.133	1.029	5524	5525	506.3	483.2
276	25	0.41	436.8	7.3	451.3	6.12	2.93	0.0059	487.9	0.135	1.083	5457	5458	505.4	482.9
291	45	0.77	403.6	13.7	451.4	3.12	0.75	0.0027	465.9	0.021	0.098	2116	2116.1	519.2	463.1
187	25	0.41	437.5	7.9	451.9	6.12	2.93	0.0059	488.6	0.134	1.049	5612	5614	507.1	483.7
193	30	0.61	429.3	18.2	461.1	5.56	2.89	0.0065	489.9	0.133	1.119	5573	5574	508.2	485.0
122	30	0.60	429.9	18.4	461.2	5.57	2.88	0.0065	490.5	0.131	1.069	5608	5609	509.5	485.7
191	30	0.61	429.9	18.7	461.7	5.57	2.90	0.0066	490.2	0.134	1.118	5565	5566	508.6	485.4
188	30	0.60	431.1	19.8	462.7	5.57	2.84	0.0064	491.5	0.128	1.025	5661	5662	511.5	486.9
214	25	0.81	412.4	-16.9	466.0	8.34	4.00	0.006	494.2	0.174	1.407	5399	5400	506.4	489.1
123	40	0.81	414.5	24.6	469.3	4.08	2.90	0.0089	488.6	0.125	0.969	5676	5677	509.9	484.6
103	25	0.65	434.7	5.0	471.7	7.27	2.50	0.0042	497.6	0.083	0.467	4193	4193	519.7	491.7
105	25	0.65	434.5	4.9	471.8	7.28	2.36	0.0037	490.2	0.065	0.283	4099	4099	522.5	487.9
213	25	0.80	418.3	-11.3	472.3	8.35	2.60	0.004	497.2	0.112	0.900	5247	5248	517.6	491.5
124	35	0.81	420.3	27.3	475.2	5.25	2.89	0.007	494.4	0.127	1.024	5682	5683	515.0	490.1
108	35	0.80	424.8	31.7	479.9	5.25	1.52	0.0036	494.6	0.059	0.420	4544	4544	533.3	490.8
110	30	0.81	426.0	14.8	481.6	6.66	1.95	0.0027	495.0	0.045	0.219	3298	3298	532.3	491.4
112	30	0.80	426.7	15.1	481.7	6.66	2.20	0.0038	491.1	0.053	0.199	3634	3634	527.2	489.3
196	30	0.81	427.0	15.8	482.5	6.65	1.92	0.0034	491.3	0.046	0.172	2685	3685	521.7	489.5
114	40	0.81	428.3	38.4	484.2	4.09	1.42	0.0044	493.6	0.060	0.470	5056	5056	536.9	490.1
121	45	0.81	427.9	38.0	484.4	3.28	1.48	0.0058	491.1	0.063	0.487	5389	5389	535.5	487.8
212	25	0.80	429.1	-0.4	484.5	8.34	2.60	0.004	503.9	0.109	0.854	5595	5596	520.3	491.7
118	40	0.82	427.7	37.9	485.7	4.08	1.46	0.0043	490.7	0.046	0.246	3862	3863	535.3	488.5
209	40	0.80	430.6	40.7	486.1	4.08	0.80	0.0025	494.0	0.034	0.265	4471	4471	563.9	490.4

The range of static wet bulb temperatures of the Icing Wedge for these ice accretion points was from 465.9 to 503.9 °R with a 5 μ particle in the flow analysis model. Note that Escort data point 291 with a Twbs of 465.9 °R did not accrete due to low IWAR (0.0027), not due to Twbs (see Figure 24). The true range of Twbs for the cases with collection, but no accretion was from 487.9 to 503.9°R. The average difference of the Twbs for these collection, but no ice accretion points was 0.7 °R below the 492 °R minimum threshold Twbs of the Icing Wedge, with a range of 16 °R. The static wet bulb temperature (Twbs) versus IWAR for the cases with hard ice accretion and ones which had collection, but no ice accretion, are plotted in Figure 24.

For the data point that experienced neither ice accretion nor ice collection, except a slight amount of ice at the support strut leading edge, the key parameters are listed in Table 6 and in Appendix C of Reference 17.

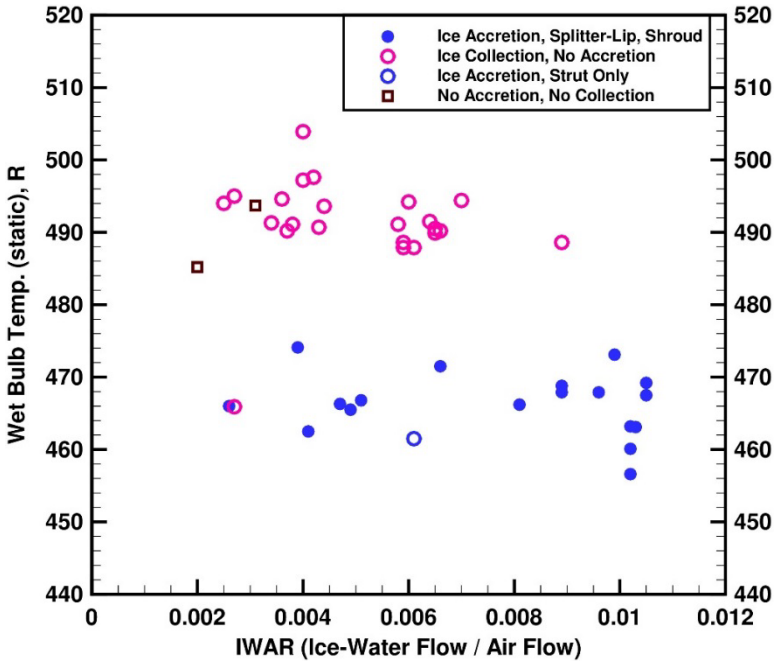

Figure 24.—The static wet bulb temperature (Twbs) versus IWAR in the splitter-shroud region, for the cases with hard ice accretion and ones which had only collection, but no ice accretion (from Table 4 and Table 5).

TABLE 6.—SPLITTER-SHROUD: NO ICE ACCRETION, EXCEPT AT SUPPORT STRUT (LOW Twbs)

Escort data point	Altitude, K ft	Flight Mach	Ambient temp., °R	Delta ISA, °R	Tt PSL Station 1 ice cloud ON, °R	Pt PSL Station 1, psia	Ice Water Content (IWC)	IWAR	Twbs splitter, shroud, fan core (6), 5 μ	Ice mass flow into core, lbm/sec	Kinetic energy heat flux, Qk	Conduct heat flux, Qc, BTU/Hr	Total heat flux, Qt, BTU/Hr	T wall core after 60s (6) 2.1, °R	T ice particle (6) 2.1, °R
289	36	0.61	413.5	23.4	443.9	4.21	2.41	0.0061	461.5	0.050	0.147	2324	2324	485.3	459.6

Figure 25 illustrates a data point of Table 6 where there was no ice accretion on the splitter-shroud region, however some ice at the strut leading edge appears to accrete. The static wet bulb temperature is 31 °R below the Icing wedge minimum threshold temperature of 492 °R. It is hypothesized that even the heat flux from the splitter-shroud wall was not adequate to melt the particle at those operating conditions. However, a small amount of ice was noted on the strut leading edge, which may have a higher heat flux at this discrete circumferential location (shown in Figure 24 by blue open circles). The calculated static wet bulb temperature distribution for this data point is illustrated in Figure 26. This data point is represented by the blue open circle in Figure 15 and Figure 21.

Figure 25.—Ice did not collect on the splitter-lip or the shroud, at data point. (Escort 289).

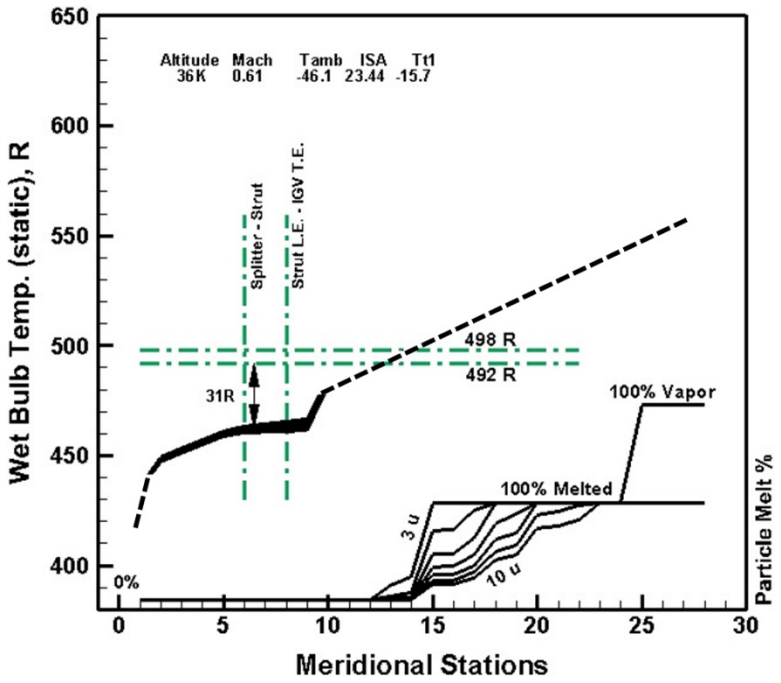

Figure 26.—Ice accretion did not occur in Escort 289 which had a static wet bulb temperature 31 °R below the Icing Wedge minimum threshold of 492 °R.

TABLE 7.—SPLITTER-SHROUD: NO ICE ACCRETION (CALCULATED HOT WALL)

Escort Data Point	Altitude, K ft	Flight Mach	Ambient temp., °R	Delta ISA, °R	Tt PSL Station 1 ice cloud ON, °R	Pt PSL Station 1, psia	Ice Water Content (IWC)	IWAR	Twbs splitter, shroud, fan core (6), 5 μ	Ice Mass flow into core, lbm/sec	Kinetic energy heat flux, Qk	Conduct heat flux, Qc, BTU/Hr	Total heat flux, Qt, BTU/Hr	T wall core after 60s (6) 2.1, °R	T ice particle (6) 2.1, °R
159	45	0.76	424.6	34.7	473.6	3.12	0.50	0.002	485.2	0.021	0.153	3581	3581	578.4	481.7
208	40	0.83	427.3	37.4	485.6	4.08	1.00	0.0031	493.7	0.042	0.332	4829	4829	553.5	490.1

For data points that experienced no ice accretion or ice collection, the key parameters are listed in Table 7. These two data points were considered to have wall temperatures that were too warm to support ice accretion, as shown by brown square symbols in Figure 24. Note that for Escort 159, there may be two reasons for no accretion: the IWAR was low, as well as the calculated Twbs was excessively high, considering the additional source of heat flux from the shroud wall.

5K ft Altitude

The calculated wall temperatures and static wet bulb temperatures at 5K ft altitude for data points with accretion and no accretion, versus IWAR are plotted in Figure 27. The calculated wall temperatures for the 5K ft points with ice accretion appear to be near, or slightly below the calculated wall temperatures for the high altitude points with ice accretion.

The video image illustrating the ice accretion points on the splitter-lip and shroud for Escort data point 243 is illustrated in Figure 28.

Figure 29 illustrates the static wet bulb temperature distribution for Escort points 243 through the full fan, the fan-core and the four stage axial compressor, as well as the particle melt ratio over a range of particle size for 3 to 10 μ. Ice accretion occurred at the stator-shroud region at a wet bulb temperature 15 °R below the Icing Wedge minimum threshold.

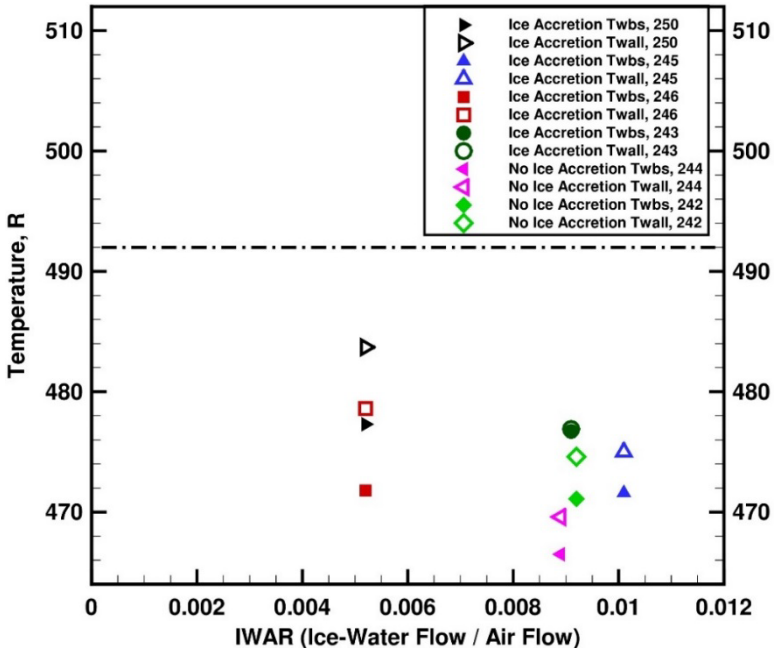

Figure 27.—Calculated wall temperature and the static wet bulb temperature at the splitter–shroud wall region at 5K ft altitude for ice accretion and no ice accretion data points (from Table 8 and Table 9).

Figure 28.—Splitter-shroud: 5K altitude ice accretion on splitter-lip and shroud for Escort data point 243.

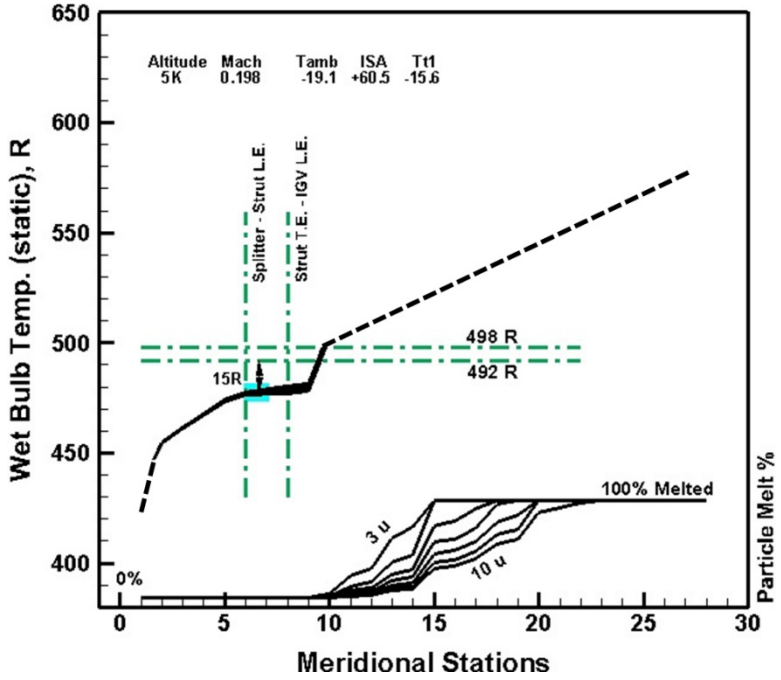

Figure 29.—The static wet bulb temperature distribution and particle melt ratio for the 5K ft altitude Escort point 243 through the full fan, the fan-core and the four stage axial compressor, as well as the particle melt ratio.

For data points that experienced ice accretion at the 5K ft altitude, the key parameters are listed in Table 8, and are illustrated by the filled green circles in Figure 30.

Table 9 lists the key parameters associated with the 5K ft altitude data points that did not have ice accretion, and are illustrated by the green open circles in Figure 30.

TABLE 8.—SPLITTER-SHROUD: 5K ALTITUDE; ICE ACCRETION

Escort data point	Altitude, K ft	Flight Mach	Ambient temp., °R	Delta ISA, °R	Pt PSL Station 1, psia	Ice Water Content (IWC)	IWAR	Twbs splitter, shroud, fan core (6), 5 μ	Ice mass flow into core, lbm/sec	Kinetic energy heat flux, Qk	Conduct heat flux, Qc, BTU/Hr	Total heat flux, Qt, BTU/Hr	T wall core after 60s (6) 2.1, °R	Tt2 Stg 2 (10), °R	T ice particle (6) 2.1, °R
250	5	0.20	432.8	-68.3	12.61	5.90	0.0052	477.3	0.194	1.040	3511	3512	483.7	588.0	473.6
245	5	0.20	434.3	-66.6	12.60	12.00	0.0101	471.6	0.306	1.176	2726	2727	475.0	555.9	470.0
246	5	0.20	434.8	-66.2	12.61	6.20	0.0052	471.8	0.158	0.608	2639	2640	478.6	557.0	469.3
243	5	0.20	440.5	-60.6	12.61	10.60	0.0091	476.7	0.267	1.006	3040	3041	476.9	567.0	470.6

TABLE 9.—SPLITTER-SHROUD: 5K ALTITUDE; NO ICE ACCRETION

Escort data point	Altitude, K ft	Flight Mach	Ambient temp., °R	Delta ISA, °R	Tt PSL Station 1 ice cloud ON, °R	Pt PSL Station 1, psia	Ice Water Content (IWC)	IWAR	Twbs splitter, shroud, fan core (6), 5 μ	Ice mass flow into core, bm/sec	Kinetic energy heat flux, Qk	Conduct heat flux, Qc, BTU/Hr	Total heat flux, Qt, BTU/Hr	T wall core after 60s (6) 2.1, °R	T ice particle (6) 2.1, °R
244	5	0.19	429.8	-71.4	433.1	12.61	10.58	0.0089	466.5	0.281	1.161	2982	2983	469.6	463.7
242	5	0.21	432.9	-68.0	436.9	12.64	10.50	0.0092	471.1	0.274	1.023	2911	2912	474.6	468.7

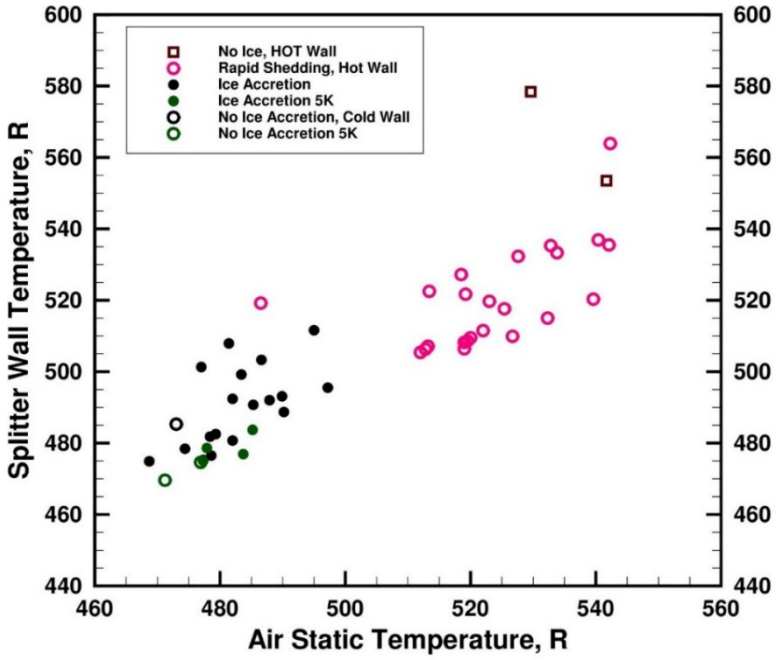

Figure 30.—Calculated wall temperature at the splitter-shroud wall region versus calculated air static temperature.

Figure 30 illustrates the strong effect of the local air static temperature on the ice accretion potential in the splitter-shroud region. The higher air temperatures result in the collection of ice on the splitter-lip, with rapid shedding a rate of several times per second, to several seconds per shed, with no accretion of hard glassy ice. However, as is evident from the data presented in the tables above there are other factors that influence ice accretion, besides the local static air temperature. Therefore, to accurately model this heat flux from the wall to the ice particle, as well as other potential heat sources, a high fidelity multi-disciplinary model of the entire front frame would be required that includes fluid dynamic analysis as well as conjugate heat transfer.

Variable Inlet Guide Vane (IGV) Region; Liquid Water From Upstream Source

As in the splitter-lip-shroud region, the Icing Wedge thresholds are likewise not applicable in the IGV region as an indicator of accretion risk. This is likewise due to the additional heat flux through the wall at the splitter-lip-shroud region that may provide liquid water to the IGV. During accretion on the IGV, the calculated Twbs were from 33.4 to 19.4 °R below freezing, and the calculated static air temperatures were from 4 to 23 °R below freezing, and the measured metal temperature of the IGV was from 492 to 488 °R. Accretion on the IGV appeared to be a function of IWAR for all operating points as shown in Figure 31. For all test points the minimum limit for ice accretion had IWAR values above 0.008. Above this value of IWAR ice accretion occurred at low fan speeds near 7300 and 6300 RPM, and are illustrated in Figure 31 by the black circles, and the values of key parameters are listed in Table 10. These were operating points where ice accretion was observed to build on the IGV without shedding. There were also operating points where the ice did not accrete, but collected briefly and rapidly shed at the IGV leading edge. These points are represented by delta symbols in Figure 31. For IWAR values less than 0.008, no accretion or collection occurred for any of the data points which were confirmed by video, as shown by the red square symbols in Figure 31.

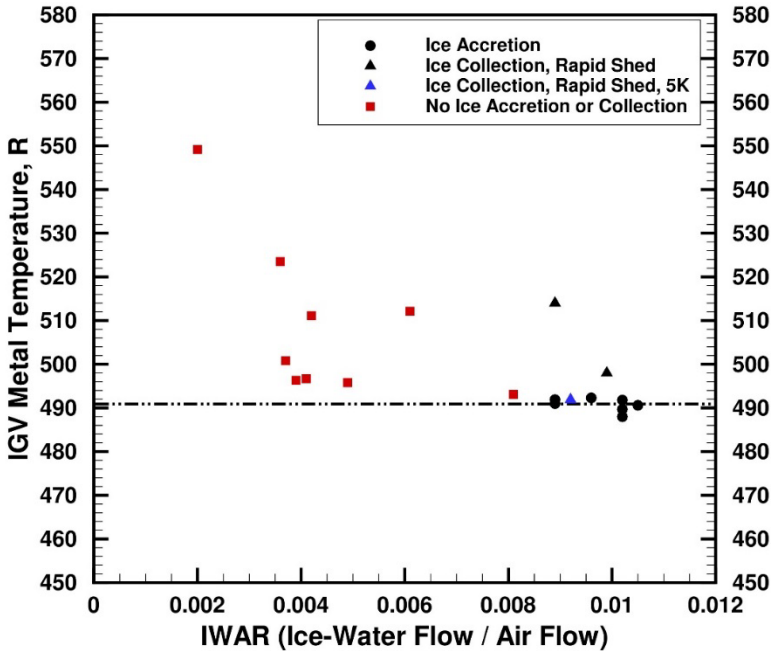

Figure 31.—Measured IGV metal temperatures versus IWAR for all operating points with video confirmation.

TABLE 10.—INLET GUIDE VANE: ICE ACCRETION; *VIDEO CONFIRMATION*

Escort data point	Altitude, K ft	Flight Mach	Ambient temp., °R	Delta ISA, °R	Tt PSL Station 1 ice cloud ON, °R	Pt PSL Station1, psia	Ice Water Content (IWC)	IWAR	T wall core after 60s (6) 2.1, °R	Twbs, IGV Station 8	Melt ratio, Station 8	T-ice particle IGV 2.5 (8) COMDES, °R	T-metal IGV 2.5 Pre ice, °R	T - metal IGV 2.5 Post ice; 60s, °R
284	36	0.61	412.8	22.9	443.4	4.21	4.10	0.0105	480.7	469.6	0.000	470.8	502.1	490.6
295	45	0.77	403.1	13.2	450.5	3.13	2.95	0.0102	481.8	465.5	0.000	465.5	496.5	488.0
300	45	0.77	388.3	-1.6	434.2	3.11	2.95	0.0102	474.9	458.6	0.000	458.7	497.3	489.7
299	45	0.77	392.8	2.9	439.4	3.12	2.92	0.0102	478.4	462.2	0.000	462.3	503.0	491.8
156	45	0.77	403.6	13.7	451.0	3.13	2.73	0.0096	492.0	470.2	0.000	470.4	511.2	492.3
280	25	0.60	411.1	-18.5	441.0	6.98	5.80	0.0089	476.5	470.5	0.000	470.7	496.2	491.0
279	25	0.60	410.1	-19.6	439.7	6.98	5.80	0.0089	475.3	470.5	0.000	470.6	494.2	491.9
242	5	0.21	432.9	-68.0	436.9	12.64	10.50	0.0092	474.6	472.6	0.000	472.9	491.6	491.9

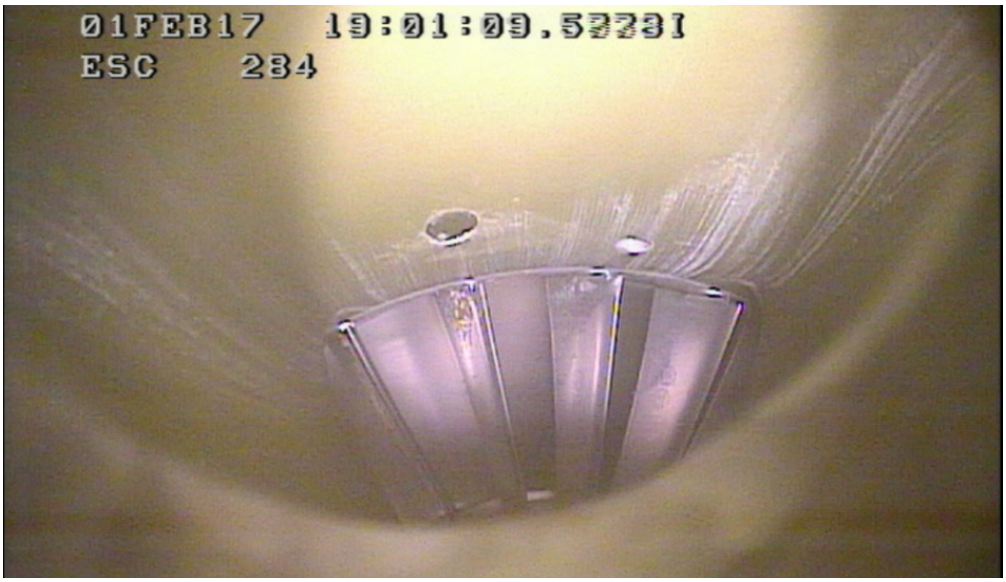

Figure 32.—Ice accretion on the IGV surface near the tip (Escort 284 at 36K ft altitude).

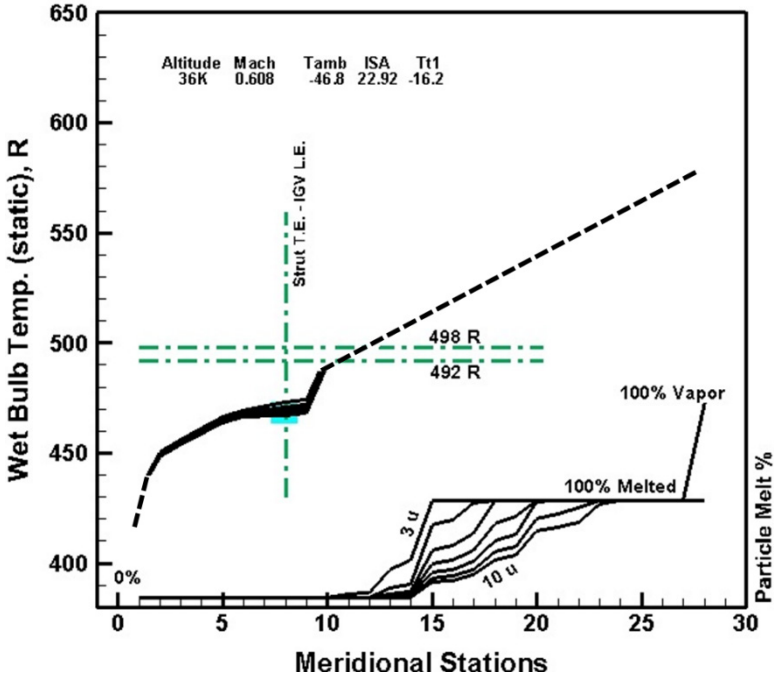

Figure 33.—The static wet bulb temperature distribution and particle melt ratio for the 36K ft altitude Escort point 284 through the fan-core and the four stage axial compressor, as well as the particle melt ratio.

The key parameters for the Escort data points with ice accretion on the IGV are listed in Table 10, and the complete analysis results are listed in Appendix C of Reference 17. An example of one operating point (Escort 284) with ice accretion on the IGV is illustrated in Figure 32.

Figure 33 illustrates the static wet bulb temperature distribution for Escort points 284 through the fan-core and the four stage axial compressor, as well as the particle melt ratio over a range of particle size for 3 to 10 μ. Ice accretion occurred at the IGV near the tip at a wet bulb temperature that was 22.4 °R below the Icing Wedge minimum threshold (492 °R).

Ice collection and rapid shedding was observed on the IGV during two test data points (123, 153) at measured metal temperatures that were well above freezing, and are illustrated with black delta symbols in Figure 31, and summarized in Table 11. While the value of IWAR for these two data points was above 0.008, the engine the local values of static air temperature were significantly higher than the air temperatures for the points with ice accretion. The higher static air temperatures at the IGV for these two data points are caused by higher inlet total air temperatures at Station 1 as well as significantly higher fan speeds. At these two operating conditions the ice collected on the IGV leading edge and rapidly shed, as shown in Figure 34.

Figure 35 illustrates the static wet bulb temperature distribution for Escort points 123 through the fan-core and the four stage axial compressor, as well as the particle melt ratio over a range of particle size for 3 to 10 μ. Ice collection and rapid shedding occurred at the IGV leading edge near the tip at a wet bulb temperature that was within the Icing Wedge minimum threshold. No ice accretion occurred.

Through video confirmation it was observed that with IWAR values less than 0.008, no ice accretion occurred on the IGV, only ice collection at the 5K ft altitude point. These operating points are shown by the red square symbols in Figure 31 and the values of the key parameters are listed in Table 12, as well as in Appendix C of Reference 17.

TABLE 11.—INLET GUIDE VANE: ICE COLLECTION WITH RAPID SHEDDING; *VIDEO CONFIRMATION*

Escort data point	Altitude, K ft	Flight Mach	Ambient temp., °R	Delta ISA, °R	Tt PSL Station 1 ice cloud ON, °R	Pt PSL Station1, psia	IWAR	T wall core after 60s (6) 2.1, °R	Twbs, IGV Station 8	Melt ratio, Station 8	T-ice particle IGV 2.5 (8) COMDES, °R	T-metal IGV 2.5 Pre ice, °R	T-metal IGV 2.5 Post ice; 60s, °R
153	45	0.81	399.4	9.5	452.2	3.28	0.0099	495.5	475.5	0.000	475.8	522.6	498.0
123	40	0.81	414.5	24.6	469.3	4.08	0.0089	509.9	490.7	0.159	491.7	556.6	514.0

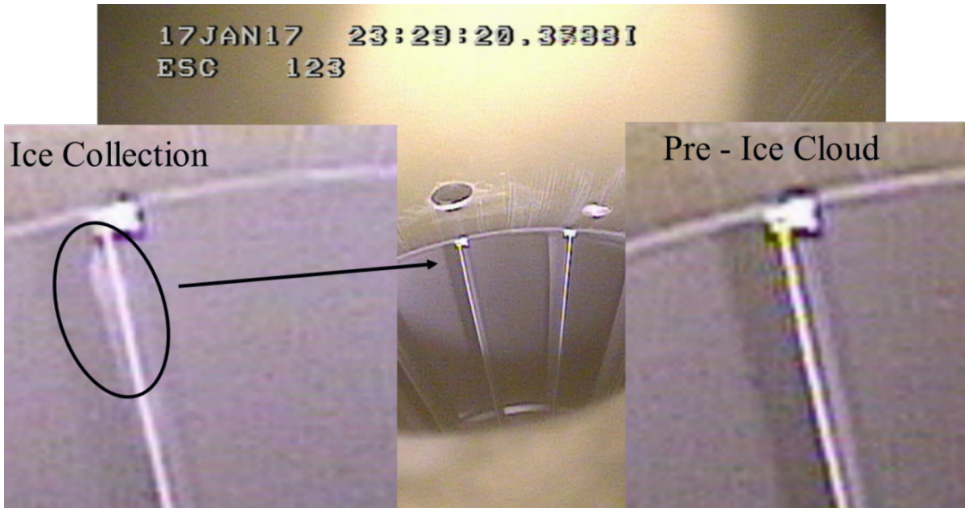

Figure 34.—Ice collection on the IGV leading edge near the tip with rapid shedding (Escort 123 at 40 K ft altitude).

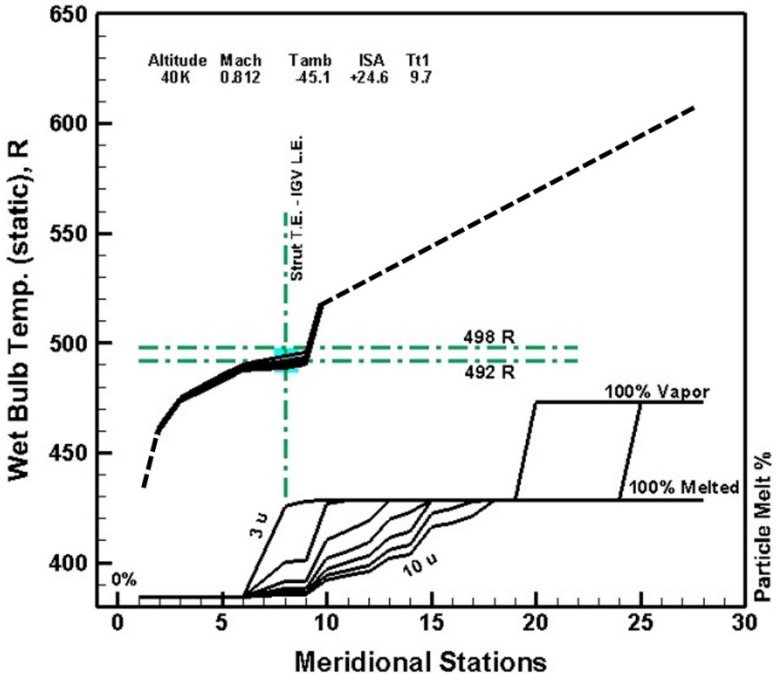

Figure 35.—The static wet bulb temperature distribution and particle melt ratio for the 40K ft altitude Escort point 123.

TABLE 12.—INLET GUIDE VANE: NO ICE COLLECTION—NO ICE ACCRETION; *VIDEO CONFIRMATION*

Escort data point	Altitude, K ft	Flight Mach	Ambient temp., °R	Delta ISA, °R	Tt PSL Station 1 Ice cloud ON, °R	Pt PSL Station 1, psia	Ice Water Content (IWC)	IWAR	T wall core after 60s (6) 2.1, °R	Twbs, IGV Station 8	Melt ratio, Station 8	T-ice particle IGV 2.5 (8) COMDES, °R	T-metal IGV 2.5 Pre ice, °R	T-Metal IGV 2.5 Post ice; 60s, °R
293	45	0.77	402.8	12.9	450.5	3.12	2.28	0.0081	490.7	468.1	0.000	468.3	511.3	493.1
100	25	0.40	436.7	10.4	450.9	5.86	2.93	0.0061	506.3	490.2	0.121	491.2	538.5	512.1
149	40	0.61	406.9	17.0	437.7	3.49	1.54	0.0049	499.2	466.8	0.000	466.8	510.4	495.8
103	25	0.65	434.7	5.0	471.7	7.27	2.50	0.0042	519.7	496.1	0.508	491.7	543.7	511.1
147	40	0.62	397.8	7.9	428.5	3.49	1.28	0.0041	501.3	463.7	0.000	463.8	507.2	496.7
157	36	0.61	422.3	32.4	453.6	4.18	1.46	0.0039	511.6	475.3	0.000	475.4	515.4	496.3
105	25	0.65	434.5	4.9	471.8	7.28	2.36	0.0037	522.5	491.4	0.110	491.7	529.5	500.8
108	35	0.80	424.8	31.7	479.9	5.25	1.52	0.0036	533.3	495.6	0.555	491.7	560.8	523.5
159	45	0.76	424.6	34.7	473.6	3.12	0.50	0.002	578.4	486.0	0.000	486.8	560.2	549.2

Figure 36 illustrates the computed ice particle temperature and measured IGV metal temperatures, 60 sec after the ice cloud was turned on, versus IWAR. The black and blue symbols represent ice accretion or collection as confirmed by video. The red symbols represent data points without ice accretion, as confirmed by video. Note that the calculated particle temperatures do not include the enthalpy rise that was transferred to the particle from the heat flux through the wall, near the splitter-shroud region upstream of the IGV. Therefore the calculated particle temperatures in Figure 36 to Figure 39 are significantly below the measured IGV metal temperature, which is near freezing for most data points where ice accreted on the IGV.

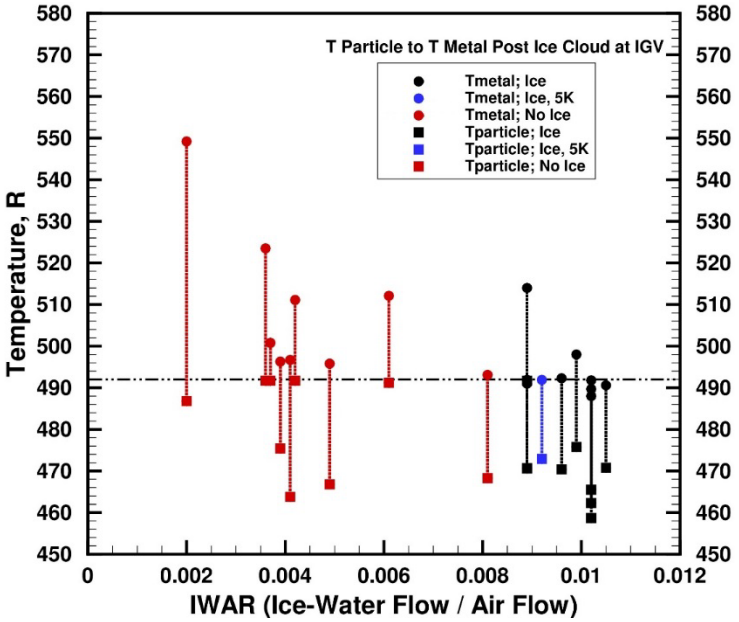

Figure 36.—Computed ice particle temperature and measured IGV metal temperatures versus IWAR. The black and blue symbols represent ice accretion or collection. The red symbols represent points without ice accretion.

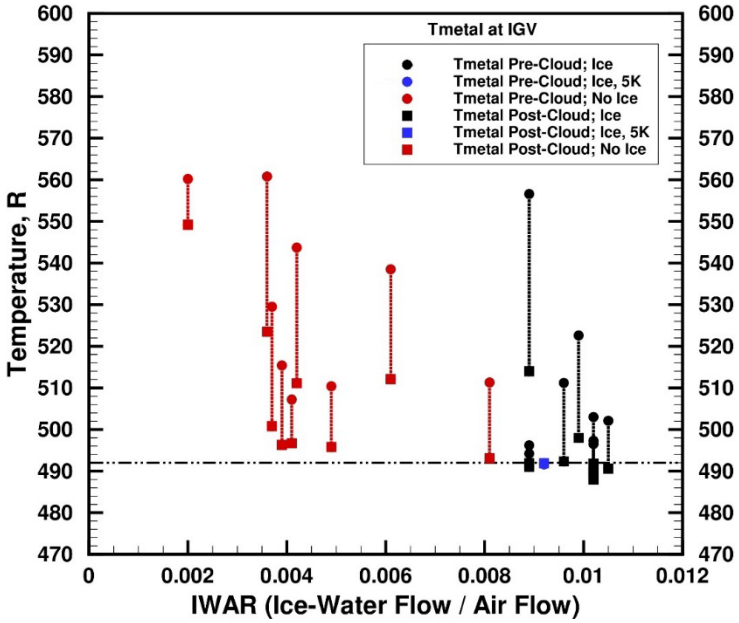

Figure 37.—Measured IGV metal temperatures pre and post ice cloud on versus IWAR. The black and blue symbols represent ice accretion or collection. The red symbols represent data points without ice accretion.

Figure 37 illustrates the measured IGV metal temperatures pre and post ice cloud on versus IWAR. In most cases, the measured IGV metal temperature reduced significantly after the ice cloud was turned on. The black and blue symbols represent ice accretion or collection as confirmed by video. The red symbols represent data points without ice accretion, as confirmed by video.

Figure 38 illustrates the computed static air temperature at the IGV and the measured IGV metal temperatures, versus IWAR. The black and blue symbols represent ice accretion or collection as confirmed by video. The red symbols represent data points without ice accretion, as confirmed by video.

Figure 39 illustrates the computed static air temperature and the computed ice particle temperature versus IWAR. The black and blue symbols represent ice accretion or collection as confirmed by video. The red symbols represent data points without ice accretion, as confirmed by video.

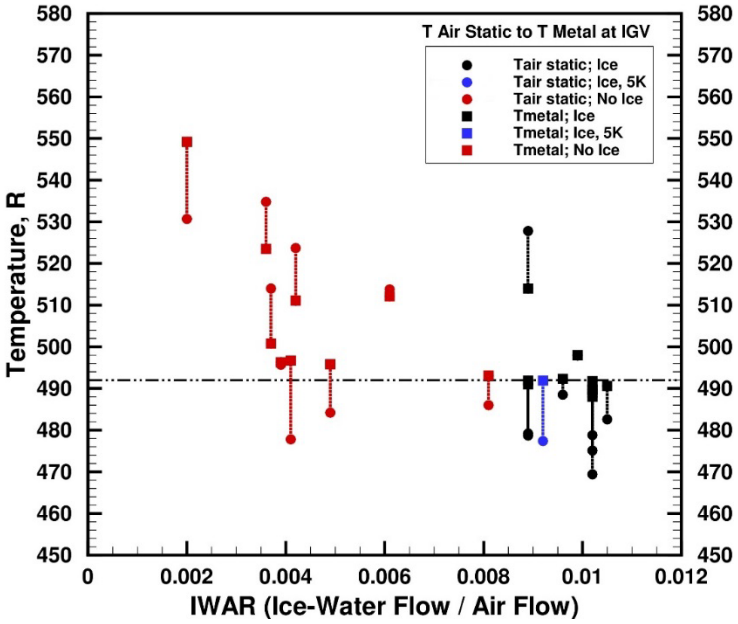

Figure 38.—Computed static air temperature and measured IGV metal temperatures versus IWAR. The black and blue symbols represent ice accretion or collection. The red symbols represent data points without ice accretion.

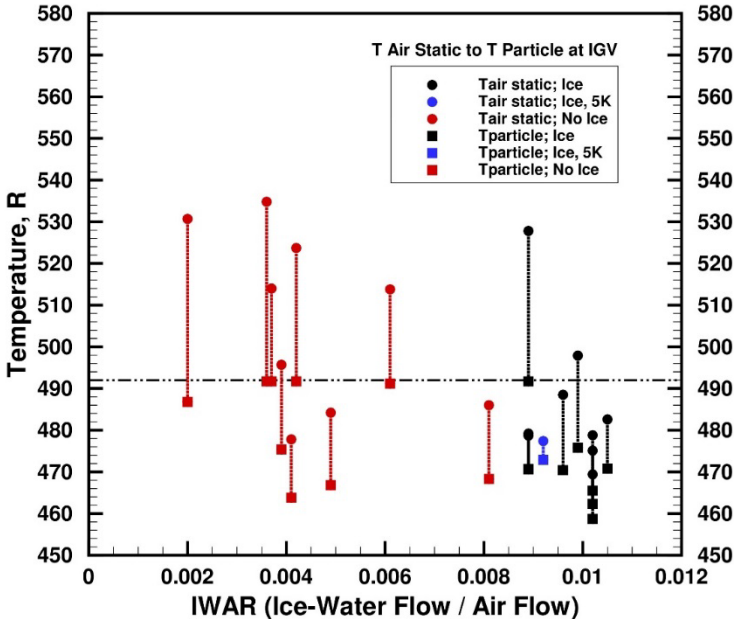

Figure 39.—Computed static air temperature and ice particle temperatures versus IWAR after ice cloud on. The black and blue symbols represent ice accretion or collection. The red symbols are data points without ice accretion.

The remaining data points that were analyzed had no video available to confirm whether there was any ice accretion or collection on the IGV. The key calculated and measured parameters for these data points are listed in Table 13, and the complete flow analysis results are listed in Appendix C of Reference 17.

TABLE 13.—INLET GUIDE VANE: NO VIDEO AVAILABLE FOR CONFIRMATION

Escort	Altitude, K ft	Flight Mach	Ambient temp, °R	Delta ISA, °R	Tt PSL Station 1 tce cloud ON, °R	Pt PSL Station 1, psia	Ice Water Content (IWC)	IWAR	T wall core after 60s (6) 2.1, °R	Twbs, IGV Station 8	Melt ratio, Station 8	T-ice particle IGV 2.5 (8) COMDES, °R	T-metal IGV 2.5 Pre Ice, °R	T-metal IGV 2.5 post ice; 60s, °R
289	36	0.61	413.5	23.4	443.9	4.21	2.41	0.0061	485.3	462.9	0.000	462.8	487.5	484.3
282	36	0.61	412.2	22.7	442.6	4.21	1.00	0.0026	507.9	466.9	0.000	466.8	500.2	493.2
287	36	0.61	412.2	22.3	443.1	4.22	2.48	0.0066	493.1	473.1	0.000	473.3	516.8	498.6
283	36	0.61	412.7	22.8	443.3	4.21	2.00	0.0051	492.4	468.1	0.000	468.1	501.1	491.0
298	45	0.78	396.2	6.4	444.2	3.14	2.95	0.0103	482.5	465.3	0.000	465.5	507.7	492.7
291	45	0.77	403.6	13.7	451.4	3.12	0.75	0.0027	519.2	466.9	0.000	466.9	511.5	498.0
292	45	0.77	403.1	13.2	451.5	3.12	1.33	0.0047	503.3	467.7	0.000	467.8	512.1	494.5
297	45	0.76	407.2	17.3	454.9	3.12	2.93	0.0105	488.7	471.6	0.000	471.8	515.3	493.2
208	40	0.83	427.3	37.4	485.6	4.08	1.00	0.0031	553.5	494.6	0.556	491.7	574.1	535.1
276	25	0.41	436.8	7.3	451.3	6.12	2.93	0.0059	505.4	490.3	0.134	491.3	539.4	511.2
187	25	0.41	437.5	7.9	451.9	6.12	2.93	0.0059	507.1	490.8	0.159	491.7	539.6	510.0
193	30	0.61	429.3	18.2	461.1	5.56	2.89	0.0065	508.2	491.6	0.242	491.7	548.6	515.5
122	30	0.60	429.9	18.4	461.2	5.57	2.88	0.0065	509.5	491.9	0.260	491.7	548.2	510.5
191	30	0.61	429.9	18.7	461.7	5.57	2.90	0.0066	508.6	491.8	0.256	491.7	548.4	517.0
188	30	0.60	431.1	19.8	462.7	5.57	2.84	0.0064	511.5	492.9	0.318	491.7	549.2	509.3
214	25	0.81	412.4	-16.9	466.0	8.34	4.00	0.006	506.4	495.5	0.442	491.7	548.7	509.0
213	25	0.80	418.3	-11.3	472.3	8.35	2.60	0.004	517.6	498.2	0.615	491.7	555.1	525.4
124	35	0.81	420.3	27.3	475.2	5.25	2.89	0.007	515.0	495.9	0.543	491.7	560.8	521.9
110	30	0.81	426.0	14.8	481.6	6.66	1.95	0.0027	532.3	495.8	0.552	491.7	546.2	508.2
112	30	0.80	426.7	15.1	481.7	6.66	2.20	0.0038	527.2	492.4	0.190	491.7	531.6	499.3
196	30	0.81	427.0	15.8	482.5	6.65	1.92	0.0034	521.7	492.5	0.202	491.7	532.4	499.8
114	40	0.81	428.3	38.4	484.2	4.09	1.42	0.0044	536.9	494.7	0.552	491.7	571.0	529.8
121	45	0.81	427.9	38.0	484.4	3.28	1.48	0.0058	535.5	492.5	0.387	491.7	574.7	529.9
212	25	0.80	429.1	-0.4	484.5	8.34	2.60	0.004	520.3	504.8	1.000	501.2	567.7	534.2
118	40	0.82	427.7	37.9	485.7	4.08	1.46	0.0043	535.3	492.1	0.260	491.7	555.1	512.0
209	40	0.80	430.6	40.7	486.1	4.08	0.80	0.0025	563.9	494.8	0.579	491.7	574.5	539.7
244	5	0.19	429.8	-71.4	433.1	12.61	10.58	0.0089	469.6	467.8	0.000	468.2	487.7	489.3
250	5	0.20	432.8	-68.3	436.2	12.61	5.90	0.0052	483.7	478.7	0.000	479.2	504.7	495.9
245	5	0.20	434.3	-66.6	437.9	12.60	12.00	0.0101	475.0	473.1	0.000	473.5	492.6	491.8
246	5	0.20	434.8	-66.2	438.4	12.61	6.20	0.0052	478.6	472.9	0.000	473.2	492.5	491.3
243	5	0.20	440.5	-60.6	444.0	12.61	10.60	0.0091	476.9	478.3	0.000	478.6	498.6	493.3

There was no direct measurement of the metal temperatures near the splitter-shroud region, however the calculated metal temperatures there were compared to the measured metal temperatures at the IGV and are shown in Figure 40. Included on the plot is a reference line (black dash-dot line) depicting a line with a slope of 1 for the two temperatures, as well as a linear least squares curve fit of the calculated splitter-shroud metal temperatures (blue dashed line). The trend of the calculated wall metal temperature closely tracks the measured IGV metal temperature. This indicates that the calibrated heat transfer model of the splitter-shroud region is adequate for comparison of calculated wall temperatures at the various test points.

HPC Stage 1 Stator Region; Liquid Water from Upstream Source

For certain operating points in the test matrix, ice was expected to accrete on HPC stage 1 stator based on the pre-test analyses. However, during testing it appeared that ice did not accrete there, since the measured metal temperatures of the variable stator were 61.6 to 79.8 °R above freezing, as shown in Table 14. This was possibly due to additional heat conducted to the particles from the upstream splitter-lip and shroud wall. In addition the energy imparted by HPC rotor 1 further increased the air temperature, thus raising the temperature of the particle entering stator 1. Note that there were no video cameras in this region.

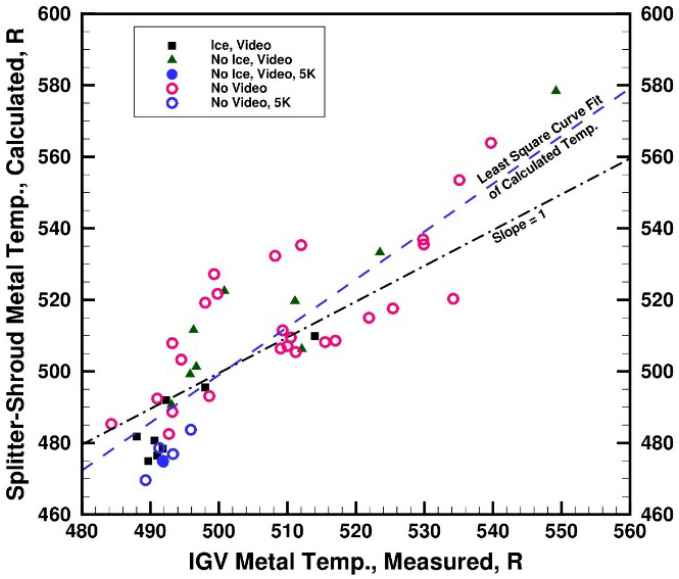

Figure 40.—Comparison of the IGV measured metal temperature to the calculated metal temperature at the splitter-shroud region. The trend of the calculated metal temperature closely tracks the measured IGV metal temperature.

TABLE 14.—HPC STAGE 1; STATOR: NO VIDEO AVAILABLE FOR CONFIRMATION

Escort data point	Altitude, K ft	Flight Mach	Ambient temp., °R	Delta ISA, °R	Tt PSL Station 1 ice cloud ON, R	Pt PSL Station 1, psia	Ice Water Content (IWC)	IWAR	Twbs, HPC Stator 1 Stat. 13	T-metal HPC Stator 1, pre ice, °R	T-Metal IGV 2.5 Post Ice; 60s, °R
153	45	0.81	399.4	9.5	452.2	3.28	2.90	0.0101	509.1	631.1	553.6
149	40	0.62	437.7	17.0	406.8	3.49	1.54	0.0049	501.8	623.0	566.8
157	36	0.61	453.6	32.4	422.1	4.18	1.46	0.0040	506.4	614.3	571.8

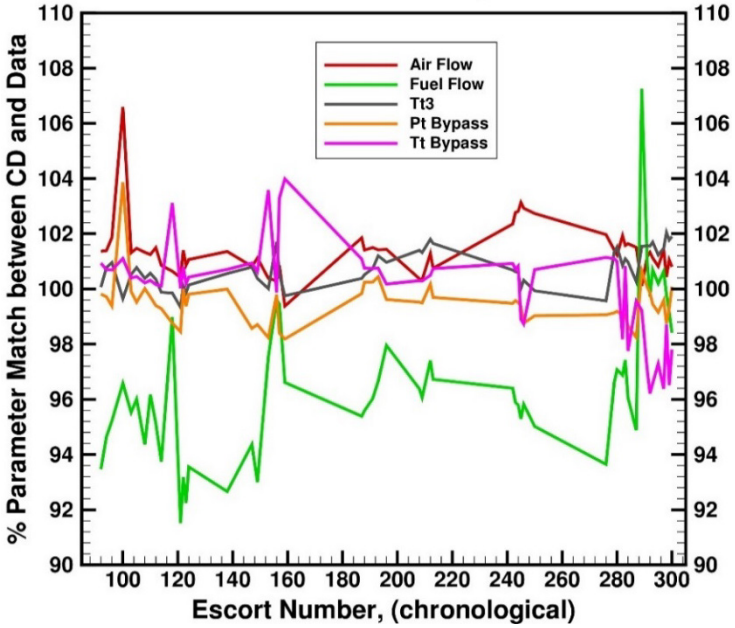

Figure 41.—Percentage difference between the CD model and the Escort test data as a function of Escort number.

Uncertainty

Key HURE engine performance parameters from the CD system model were compared to the Escort measurement data in order to validate the model. Figure 41 illustrates the percentage difference of the parameters between the measured data and the CD as a function of Escort data number, which increased chronologically. Variances of up to 6 percent were noted for certain engine performance parameters. The analysis conducted in this study is based on the CD estimate of the flow through the core. These differences may affect the analysis results with COMDES-MELT, thus adding to the uncertainty.

The current mean-line flow analytical capability for calculating the values of the key icing parameters lacks the radial distribution at the blade row edges. Thus its accuracy for estimating the span wise location of accretion along the fan-stator needs to be improved, or higher fidelity modeling needs to be implemented.

Future Work

A higher fidelity computational capability (two-dimensional streamline curvature flow analysis, or full three-dimensional CFD) is required in order to calculate the values of the key icing parameters through the span of a blade/stator at multiple radial locations. Additionally, the heat flux through the non-adiabatic walls can be a major factor in ice accretion. The differences between the CD model and the measured Escort data need to be reconciled. This would also reduce the uncertainty of the COMDES-MELT model, which relies on input from both. The measurement uncertainty can be decomposed into the sampling uncertainty and the systematic uncertainty. For example, the sampling uncertainty can be due to variations in altitude, inlet temperature, fan speed and flight Mach number between test data points. The systematic uncertainty can be caused by possible measurement errors in the instrumentation and data acquisition. All the measurement uncertainties can propagate which cause variation in the accuracy of the model.

Summary/Conclusions

The Honeywell Uncertified Research Engine (HURE) has been tested in the Propulsion System Laboratory (PSL) at NASA Glenn Research Center with ice crystal cloud ingestion over a range of simulated altitudes, ambient temperatures, and engine operating conditions (varying flight Mach number and fan speed).

A computational process utilizing the mean-line (COMDES-MELT) aerodynamic compressor flow analysis code along with the Honeywell provided customer deck were utilized for the post-test analysis of the engine test data.

The HURE engine testing indicates that ice accretion occurred differently in the fan-stator, than it does near the splitter-lip and shroud region, as well as on the compressor inlet guide vane.

- Ice accretion on the non-metallic fan-stator vanes occurs within the range of wet bulb temperature thresholds of the Icing Wedge (492 to 498 °R) where it was expected to occur, and did not have any icing when the Twbs was outside these Icing Wedge thresholds. The accretion here appears to be an adiabatic process. In the fan-stator region the static wet bulb temperature thresholds of the Icing Wedge, proved to have a 94 percent accuracy as an indicator of icing risk. Although the mean-line flow analytical capability lacks the radial distribution of particles, and key icing parameters, it can be an effective tool for estimating their bulk values.
- Early during the testing phase of the HURE, real-time analysis of the data indicated that the splitter-lip and shroud region of the gooseneck may have been heated, however the heat source was not well understood. The PSL test plan was adjusted accordingly for subsequent test data points. In order to induce ice accretion near the splitter-shroud region, the target value of static wet bulb temperature was reduced by 24 °R to a value near 468 °R. This proved to be a successful technique for forcing ice to accrete in that region, in spite of the suspected non-adiabatic walls. During post-test analysis, a simple heat transfer model was developed in order to calculate the wall temperature in the splitter-shroud region at all operating conditions. The heat transfer model was incorporated into the compressor flow analysis code, for an order-of-magnitude calculation of wall temperature. In this non-adiabatic region, the Icing Wedge wet bulb temperature thresholds were not applicable as an indicator of icing risk due to the additional heat flux through the walls.
- The ice accretion on the variable inlet guide vanes (IGV) of the compressor appeared to be a strong function of the IWAR (ice-water flow rate to air flow rate ratio). Ice accretion on the IGV occurred at values of IWAR above 0.008, whereas no ice accretion on the IGV occurred below that value. In the IGV region, the Icing Wedge thresholds were not applicable as an indicator of icing risk due to the source of liquid water from upstream (splitter-lip-shroud).
- Non-adiabatic compressor flow path walls require a fully coupled multidisciplinary analysis of the conjugate heat transfer through the walls, the air flow, as well as the thermodynamic state of the ice particle, in order to determine the static wet bulb temperature distribution in the flow field.

References

1. Mason, J. G., Chow, P., Fuleki, D. M., “Understanding Ice Crystal Accretion and Shedding Phenomenon in Jet Engines Using a Rig Test,” GT2010-22550.
2. Mason, J. G., Grzych, M., “The Challenges Identifying Weather Associated With Jet Engine Ice Crystal Icing,” SAE 2011-38-0094.
3. Goodwin, R. V., Dischinger, D. G., “Turbofan Ice Crystal Rollback Investigation and Preparations Leading to Inaugural Ice Crystal Engine Test at NASA PSL-3 Test Facility,” AIAA 2014-2895.
4. Oliver, M. J., “Validation Ice Crystal Icing Engine Test in the Propulsion Systems Laboratory at NASA Glenn Research Center,” AIAA-2014-2898.
5. Flegel, A. B., Oliver, M. J., “Preliminary Results from a Heavily Instrumented Engine Ice Crystal Icing Test in a Ground Based Altitude Test Facility,” AIAA-2016-3894.
6. Struk, P., Lynch, C. J., “Ice Growth Measurements from Image Data to Support Ice-Crystal and Mixed-Phase Accretion Testing,” AIAA 2012-3036.
7. Bartkus, T. P., Tsao, J. C., Struk, P. M., Van Zante, J. F., “Numerical Analysis of Mixed-Phase Icing Cloud Simulations in the NASA Propulsion Systems Laboratory,” 8th AIAA Atmospheric and Space Environments Conference, 13-17 June, 2016, Washington D.C., AIAA.
8. Veres, J. P., Jorgenson, P. C. E., “Prediction and Analysis of Ice Accretion in a Research Turbofan Engine With Ice Crystal Cloud Ingestion at Simulated Altitudes,” NASA/TM—2017-219724 (availability restricted to U.S. government and NASA contractors)
9. Veres, J. P., “Axial and Centrifugal Compressor Mean Line Flow Analysis Method,” AIAA-2009-1641, NASA/TM—2009-215585.
10. Veres, J. P., Jorgenson, P. C. E., Wright, W. B., Struk, P., “A Model to Assess the Risk of Ice Accretion due to Ice Crystal Ingestion in a Turbofan Engine and its Effects on Performance,” AIAA 2012-3038.
11. Veres, J. P., Jorgenson, P. C. E., “Modeling Commercial Turbofan Engine Icing Risk with Ice Crystal Ingestion,” AIAA 2013-2679.
12. Veres, J. P., Jorgenson, P. C. E., Coennen R., “Modeling Commercial Turbofan Engine Icing Risk with Ice Crystal Ingestion; Follow-On,” AIAA-2014-2899.
13. Jorgenson, P. C. E., Veres, J. P., Jones, S. M., “Modeling the Deterioration of Engine and Low Pressure Compressor Performance During a Roll Back Event due to Ice Accretion,” AIAA-2014-3842.
14. Veres, J. P., Jones, S. M., Jorgenson, P. C. E., “Performance Modeling of Honeywell Turbofan Engine Tested with Ice Crystal Ingestion in the NASA Propulsion System Laboratory,” SAE-2015-01-2133.
15. Veres, J. P., Jorgenson, P. C. E., Jones, S. M, “Modeling of Highly Instrumented Honeywell Turbofan Engine Tested with Ice Crystal Ingestion in the NASA Propulsion System Laboratory,” AIAA-2016-3895.
16. Veres, J. P., Jorgenson, P. C. E., Jones, S. M., Nili, S., “Modeling of A Turbofan Engine with Ice Crystal Ingestion in the NASA Propulsion System Laboratory,” GT2017-63202.
17. Veres, J. P., Jorgenson, P. C. E., Bommireddy, S. R., Nili, S., “Analysis of the Honeywell Uncertified Research Engine (HURE) with Ice Crystal Cloud Ingestion at Simulated Altitudes (Gov’t Version),” NASA/TM—2018-220022 (availability restricted to U.S. government and NASA contractors).